Chapter 8
Nonlinear Magneto-Optics in Magnetophotonic Crystals

Oleg A. Aktsipetrov, Andrey A. Fedyanin, Mitsuteru Inoue, Miguel Levy, and Tatyana V. Murzina

Abstract The chapter surveys the results on the investigation of the nonlinear magneto-optical properties of magnetophotonic crystals (MPC) and microcavities. The effects of the second- and third-harmonics generation as well as nonlinear magneto-optical Faraday and Kerr effects are reviewed. The main magnetic material used in the MPC structures, which determines the magneto-optical activity of the magnetophotonic structures, is yttrium–iron garnet (YIG), which appears as a continuous layer in 1D MPC, microcavity layer in magnetophotonic microcavities or YIG nanoparticles incorporated in artificial opal structure. We demonstrate that many-fold amplification of the nonlinear magneto-optical effects is attained within the spectral edge of the photonic band gap and within the microcavity mode as compared to linear magneto-optical analogs. Strong light localization as well as the realization of the phase matching conditions are discussed as possible mechanisms of the observed enhancement of the nonlinear magneto-optical effects.

8.1 Introduction: Nonlinear Optics and Magneto-Optics in Photonic Band-Gap Materials

Magnetic photonic band-gap materials that are spatially periodic structures composed (at least partially) of magnetic materials, are a subject of high interest due to their unique optical and magneto-optical properties absent for bulk materials of

O.A. Aktsipetrov · A.A. Fedyanin (✉) · T.V. Murzina
Faculty of Physics, M.V. Lomonosov Moscow State University, Moscow 119991, Russia
e-mail: fedyanin@nanolab.phys.msu.ru

T.V. Murzina (✉)
e-mail: murzina@mail.ru

M. Inoue
Department of Electrical and Electronic Information Engineering, Toyohashi University of Technology, Toyohashi, Aichi 441-8580, Japan

M. Levy
Physics Department, Michigan Technological University, Houghton, MI 49931, USA

the same composition. These properties originate from the modification of the optical spectra of magnetophotonic crystals (MPC) that leads to the appearance of the photonic band gap and/or magnetophotonic microcavity (MMC) mode and to the corresponding strong changes in the light localization and dispersion. These effects, in turn, can modify drastically the spectral efficiency of optical and nonlinear optical processes.

In this chapter we mostly review the results of our recent studies of optical second- and third harmonics generation in garnet-based one-dimensional MPC and MMC, as well as in YIG-substituted artificial opals. In what follows we will demonstrate that such structures reveal many-fold amplification of the linear magneto-optical Faraday and Kerr effects as well as the second- and third-order nonlinear optical and magnetization-induced effects. These properties are very attractive for magnetic-field operation over the light flow in such structures, including that based on the nonlinear optical effects. In the latter case, in spite of a relative complicity of the nonlinear optical technique, enormously large values of the nonlinear magneto-optical effects (i.e. magnetization-induced rotation of the polarization plane or changes in the harmonics' phase and intensity) can be of practical interest as they combine high nonlinearity, photonic band gap (PBG) and magnetic properties of magnetophotonic crystals.

In order to increase an intrinsically weak efficiency of the nonlinear optical processes of the materials that constitute photonic crystals (PC), the following approach can be realized in case of MPC, namely, the possibility to fulfill the phase matching conditions in spatially periodic media. This phenomenon was pointed out by N. Bloembergen [1, 2]. As it is well known, for the case of second-harmonic generation (SHG) the phase matching conditions that provide the maximal efficiency of this nonlinear process can be written as $k_{2\omega} = 2k_{\omega} + \Delta_2 k$, where k_{ω} and $k_{2\omega}$ are the fundamental and SHG wave vectors and $\Delta_2 k$ is the phase mismatch that appears due to the dispersion of PC constituting materials. Similar conditions for the case of third-harmonic generation (THG) looks like $k_{3\omega} = 3k_{\omega} + \Delta_3 k$. In real anisotropic crystals the phase mismatch Δk can be compensated by the differences in the phase velocities of o and e waves of the corresponding wavelength. On the contrary, the condition $\Delta k = 0$ in a PC can be realized for the pump and harmonics waves of the same polarizations due to the modification of the PC dispersion in the spectral vicinity of the PBG edge. In that case the phase mismatch at the fundamental and harmonics wavelength can be compensated due to the appearance of the reciprocal lattice vector, $\mathbf{G}$, so that $\Delta_2 k = k_{2\omega} - 2k_{\omega} + \mathbf{G} = 0$. Such an enhancement of the nonlinear optical effects in non-magnetic PC was observed in a number of papers [3–5].

One more mechanism of the enhancement of the nonlinear optical effects is attributed to a strong spatial light localization in PBG structures—photonic crystals and photonic microcavities. In the latter case a many-fold enhancement of the local optical field resonant with the microcavity mode is attained due to the multiple interference and multipass character of light propagation within the MC layer. For the case of PC structures, an increase of the local density of states is realized because of the Bloch nature of the electromagnetic waves in PC. The mentioned above effects

of the amplification of the local optical fields in spatially periodic structures were realized in the reviewed works for the case of magnetophotonic structures so that a significant amplification of the nonlinear-optical magnetic effects were observed [33–36].

8.2 Nonlinear Magneto-Optics: Background

Nonlinear optics describes the interaction of intense light with a matter when the efficiency of the nonlinear-optical effects (harmonics generation, self-action of light, optical rectification and Kerr effect, CARS and many others) is a nonlinear function of the fundamental beam intensity. The variety of nonlinear optical phenomena is enlarged further in the case of magnetic structures, where additional symmetry operations can lead to the appearance of new effects in the nonlinear-optical response.

In centrosymmetric materials the magnetization vector does not break the inversion symmetry due to its axial nature. Thus even-order nonlinear-optical effects (like optical second harmonic generation), including nonlinear magneto-optical ones (like magnetization-induced SHG (MSGH)), require the lack of the inversion symmetry within the electric-dipole approximation. On the contrary, magnetization-induced effects in third-harmonic generation (MTHG) can be observed in materials of any symmetry. The electromagnetic fields at the double and triple frequencies of the fundamental radiation are induced by the quadratic and cubic nonlinear polarizations, $\mathbf{P}^{(2)}(2\omega)$ and $\mathbf{P}^{(3)}(3\omega)$, which are written (in the electric-dipole approximation) as follows:

$$\mathbf{P}^{(2)}(2\omega) = \chi^{(2)}(\mathbf{M}) : \mathbf{E}_\omega \mathbf{E}_\omega, \tag{8.1}$$

$$\mathbf{P}^{(3)}(3\omega) = \chi^{(3)}(\mathbf{M}) \vdots \mathbf{E}_\omega \mathbf{E}_\omega \mathbf{E}_\omega, \tag{8.2}$$

where $\mathbf{E}_\omega$ is the fundamental field amplitude, $\chi^{(2)}$ and $\chi^{(3)}$ are the quadratic and cubic electric-dipole susceptibility tensors of a magnetic material (i.e. garnets in our case) that forms the MPC and MMC structures. Hereafter the influence of the domain walls is neglected since all the presented effects in MSHG and MTHG are observed using saturating dc-magnetic fields providing a single-domain state of magnetic garnet films. The dependence of $\chi^{(2)}$ and $\chi^{(3)}$ tensors on the magnetization vector $\mathbf{M}$ can be written as a sum of three terms:

$$\chi^{(2)}(\mathbf{M}) = \chi^{(2,0)} + \chi^{(2,1)} \cdot \mathbf{M} + \chi^{(2,2)} : \mathbf{MM}, \tag{8.3}$$

$$\chi^{(3)}(\mathbf{M}) = \chi^{(3,0)} + \chi^{(3,1)} \cdot \mathbf{M} + \chi^{(3,2)} : \mathbf{MM}. \tag{8.4}$$

The tensors $\chi^{(2,0)}$ and $\chi^{(3,0)}$ describe the non-magnetic (crystallographic) contributions to $\chi^{(2)}$ and $\chi^{(3)}$, respectively, while the axial tensors (or pseudotensors) $\chi^{(2,1)}$ and $\chi^{(3,1)}$ induce the MSHG and MTHG contributions in $\mathbf{P}^{(2)}(2\omega)$ and $\mathbf{P}^{(3)}(3\omega)$, which are odd in the magnetization. The tensors $\chi^{(2,2)}$ and $\chi^{(3,2)}$ are responsible for the MSHG and MTHG terms that are even in $\mathbf{M}$. Non-zero tensor elements can be found when using the invariance of the susceptibility tensors under the symmetry operations valid for a particular point symmetry group of a material. Here we

necessarily have to take into account different transformation matrices for the polar and axial frames.

Yttrium–iron garnet possesses the inversion symmetry, however, thin garnet films, both epitaxial and polycrystalline, are often noncentrosymmetric. Lowering of the symmetry of initially centrosymmetric garnet lattice was concluded by observation of the magnetoelectrical effect linear in the electric field, which requires the medium with the broken inversion symmetry [11]. The lattice deformation and the variation of the lattice parameters of the polycrystalline yttrium-garnet films due to the formation of oxygen vacancies is directly obtained from X-ray diffraction analysis [12]. Numerous SHG studies in magnetic garnet films also allow breaking the YIG inversion symmetry. For example, enhancement of quadratic susceptibility of Bi-substituted YIG (Bi:YIG) films films in comparison with undoped YIG film was directly observed in reflected [13] and transmitted [14] SHG. Temperature variations of the SHG response are observed in Bi-doped garnet films grown on gadolinium-gallium garnet substrates [15, 16]. The thickness dependence of the SHG intensity from Bi:YIG films is reported in Ref. [17].

The inversion symmetry of thin Bi:YIG films is lifted since the film plane becomes mirror plane no more. Such a growth-induced film anisotropy is more likely attributed to the local distortion of the garnet cell by bismuth atoms and their ordering on nonequivalent crystallographic sites during the film growth [15]. Another source of an enhanced quadratic susceptibility of Bi:YIG films is proposed to be the lattice misfit strain in the deformed garnet layer near the substrate [12, 18] forming a polar axis along the film normal. Both mechanisms can be responsible for the inversion symmetry breaking in Bi:YIG layers in the studied MPCs and MMCs. As the garnet films used are heavily doped by bismuth atoms (one Bi atom per two Y atoms), thus large distortions in the dodecahedral rare-earth-ions sublattice of the garnet crystal cell are expected. Polar axis along the Bi:YIG film normal can be also yielded by the film sputtering on the fused quartz substrate or amorphous silicon dioxide layers and the subsequent high temperature annealing of the Bi:YIG layer with two nonequivalent, garnet–air and garnet–silicon dioxide, interfaces. Meanwhile, the description of microscopic mechanisms of the inversion symmetry breaking in Bi:YIG films remains incomplete.

We use a macroscopic description of the electric-dipole SHG sources in garnet films, which deals with appropriate symmetry elements related to the whole garnet film. Bi:YIG films are treated as layers possessing ∞m symmetry group with mirror planes perpendicular to the film plane. We will consider a Cartesian frame $\mathbf{e}_x, \mathbf{e}_y, \mathbf{e}_z$ with the xy plane perpendicular to the symmetry planes m_z so that the xy plane is the film surface and the xz plane denotes the plane of incidence. The non-zero elements of the $\chi^{(2,1)}$ and $\chi^{(3,1)}$ tensors describing the magnetization-induced quadratic and cubic polarizations, $P_i^{(2),M} = \chi_{ijkL}^{(2,1)} E_j^\omega E_k^\omega M_L$ and $P_i^{(3),M} = \chi_{ijklN}^{(3,1)} E_j^\omega E_k^\omega E_l^\omega M_N$, are shown in Table 8.1. For comparison, the non-zero elements of the $\chi^{(2,0)}$ and $\chi^{(3,0)}$ tensors that define the non-magnetic component of the quadratic and cubic polarizations, $P_i^{(2),NM} = \chi_{ijk}^{(2,0)} E_j^\omega E_k^\omega$ and $P_i^{(3),NM} =$

Table 8.1 Non-zero elements of $\chi_{ijkL}^{(2,1)}$, $\chi_{ijklN}^{(3,1)}$, $\chi_{ijk}^{(2,0)}$, and $\chi_{ijkl}^{(3,0)}$ tensors for the ∞m symmetry group divided into the magnetization vector components (columns) and polarization combinations of the fundamental and harmonic waves (rows). M_X, M_Y and M_Z relate to the longitudinal, transversal and polar nonlinear magneto-optical Kerr effect (NOMOKE) configurations. $\times 1$ denotes the columns containing non-magnetic SHG and THG contributions. m indicates the mixed polarization of the fundamental radiation, which is 45°-rotated relative to the s and p-polarizations. Last two rows contain the non-zero tensor elements, which contribute in polarization combinations with m-polarization only

	THG				SHG			
	$\times M_X$	$\times M_Y$	$\times M_Z$	$\times 1$	$\times M_X$	$\times M_Y$	$\times M_Z$	$\times 1$
$s \rightarrow s$	0	0	0	χ_{yyyy}	χ_{yyyX}	0	0	0
$s \rightarrow p$	χ_{zyyyX}	0	χ_{xyyyZ}	0	0	χ_{xyyY}	0	χ_{zyy}
$p \rightarrow s$	χ_{yxxzX}, χ_{yzzzX}	0	χ_{yxzzZ}, χ_{yxxxZ}	0	χ_{yxxX}, χ_{yzzX}	0	χ_{yxzZ}	0
$p \rightarrow p$	0	χ_{zxzzY}, χ_{xxxzY}, χ_{zxxxY}, χ_{xzzzY}	0	χ_{zzzz}, χ_{xxxx}, χ_{zxxz}, χ_{xxzz}	0	χ_{xxxY}, χ_{xzzY}, χ_{zxzY}	0	χ_{zzz}, χ_{xzx}, χ_{zxx}
$m \rightarrow s$	χ_{yyyzX}	χ_{yxyzY}	χ_{yxyyZ}	χ_{yxxy}, χ_{yyzz}	0	χ_{yxyY}	0	χ_{yzy}
$m \rightarrow p$	χ_{zxxyX}, χ_{xyzzX}, χ_{xxyzX}	χ_{zxyyY}, χ_{xyyzY}	χ_{xyzzZ}, χ_{xxxyZ}	χ_{xxyy}, χ_{zyyz}	χ_{zyzX}, χ_{xyxX}	0	χ_{xyzZ}	0

$\chi_{ijkl}^{(3,0)} E_j^\omega E_k^\omega E_l^\omega$, are presented as well. The tensor elements are divided into different columns in accordance with the magnetization direction and combinations of polarization of the fundamental and harmonics' waves.

In transparent materials, the elements $\chi^{(2,0)}$ and $\chi^{(3,0)}$ tensor elements are real values, while $\chi^{(2,1)}$ and $\chi^{(3,1)}$ tensor components are imaginary. Interference between non-magnetic and magnetization-induced components of the second harmonic (SH) and third harmonic (TH) fields which leads to the observation of odd in the magnetization effects in the SHG and THG intensity, requires absorption. This is the case of Bi:YIG films, which reveal the absorption band above 500–550 nm depending on the Bi content [19]. Bi:YIG films transparency in the red and IR regions allows the high contrast multiple interference of the fundamental radiation resulting in pronounced photonic band gap effects and fundamental field localization at the microcavity mode.

One more but equivalent approach for the description of nonlinear magneto-optical effects is based on another form of phenomenological description of the magnetization-induced nonlinear-optical susceptibility tensor. The general expression for the nonlinear polarization is as written in (8.1), while the second- and third-order susceptibility tensors are divided into odd and even in **M** parts,

$$\chi^{(2)}(\mathbf{M}) = \chi^{(2)\text{even}}(\mathbf{M}) \pm \chi^{(2)\text{odd}}(\pm\mathbf{M}), \tag{8.5}$$

$$\chi^{(3)}(\mathbf{M}) = \chi^{(3)\text{even}}(\mathbf{M}) \pm \chi^{(3)\text{odd}}(\pm\mathbf{M}), \tag{8.6}$$

where even in **M** susceptibility components include both the crystallographic and even (quadratic) in magnetization effects. Such a description was first developed in

Ref. [7] for the surfaces of a cubic crystal of different crystallographic orientations. Such formulas do not require to justify the expansion of the nonlinear polarization in powers of **M** and to estimate the corresponding small parameter.

It should be noted that non-zero tensor elements summarized in Table 8.1 or in more detail in Ref. [7] reveal the symmetry of magnetization-induced nonlinear-optical response of the surface of an isotropic or cubic medium, which can be applied to the case of iron-garnet layers. At the same time, in case of MPC or MMC the propagation effects of the fundamental and SHG waves within the YIG layers determine the SHG efficiency and should be considered when analyzing the values of the magnetization-induced SHG effects.

It stems from Table 8.1 that depending on the geometry of the application of the dc-magnetic field, magnetization-induced rotation of the SHG polarization plane (polar and longitudinal NOMOKE), or intensity and phase (transversal NOMOKE) changes of the harmonics' waves can be observed, similarly to the linear magneto-optics. At the same time, there is a difference in the values of the linear- and nonlinear magneto-optical effects (NOMOKE). In the latter case the intensity and polarization effects for typical ferromagnetic metals or dielectrics exceed magneto-optical analogs by one-two orders of magnitude, which was shown both theoretically and experimentally [6–10].

The wave equation for the fundamental, second and third harmonics can be written as

$$\mathbf{E}(j\omega) + \frac{\varepsilon(j\omega)}{c^2}\frac{d^2}{dt^2}\mathbf{E}^j(j\omega) = -\frac{1}{\varepsilon_0 c^2}\frac{d^2}{dt^2}\mathbf{P}^{(2,3)}\delta_{(2,3)j} \tag{8.7}$$

where $j = 1, 2, 3$, $\varepsilon(j\omega)$ is the dielectric function at the corresponding frequency, and second- and third-order nonlinear polarizations are the source terms. In the linear case (8.7) is homogeneous, and left- and right-circularly polarized waves are its eigen solutions. Magneto-optical effects are governed in that case by the non-diagonal components of $\varepsilon(\omega)$, or by the complex refractive indices for the circular waves $n_\pm$. For the harmonics' generation not only the $n_\pm$ at the SHG and THG wavelengths rule out the magnetic field induced effects, but $\chi^{(2,3)\text{odd}}(\mathbf{M})$ as well, which are present in the right-hand part of (8.7) and that are comparable in value with the even in magnetization terms, $\chi^{(2,3)\text{even}}$. This additional magnetic-field induced material susceptibility is mostly responsible for large values of NOMOKE.

In what follows we will mostly describe the transversal NOMOKE, i.e. magnetic-field induced changes in the SHG(THG) intensity. As a measure of this effect the SHG(THG) magnetic contrast is introduced as

$$\rho_{2\omega,3\omega} = \frac{I_{2\omega,3\omega}(+) - I_{2\omega,3\omega}(-)}{I_{2\omega,3\omega}(+) + I_{2\omega,3\omega}(-)}, \tag{8.8}$$

where the signs $+$ and $-$ denote the direction of the transversal dc-magnetic field. Taking into account that the susceptibility terms $\chi^{(2,3)\text{even}}$ and $\chi^{(2,3)\text{odd}}(\mathbf{M})$ are the sources of the corresponding SHG(THG) fields $\mathbf{E}(2\omega, 3\omega)$, the total field at the second- and third-harmonics wavelengths is expressed by the vector sum

$$I(2\omega, 3\omega) = \left|\mathbf{E}^{\text{even}}(2\omega, 3\omega) \pm \mathbf{E}^{\text{odd}}(2\omega, 3\omega)\right|^2, \tag{8.9}$$

Thus in the assumption of a small value of odd in **M** component of the SHG (THG) fields one can obtain the expression for the magnetic contrast

$$\varrho_{2\omega, 3\omega} \approx 2 \frac{E^{\text{odd}}(2\omega, 3\omega)}{E^{\text{even}}(2\omega, 3\omega)} \cos\varphi, \tag{8.10}$$

where φ is the phase shift between E^{odd} and E^{even}. Thus both the relative value $E^{\text{odd}}(2\omega, 3\omega)/E^{\text{even}}(2\omega, 3\omega)$ as well as φ determine the magnetic contrast that is measured experimentally. The latter quantity can be estimated experimentally from the SHG(THG) interferometry measurements.

8.3 Samples and Set-Ups

Magnetophotonic microcavities are formed from two dielectric Bragg reflectors and a ferrimagnetic cavity spacer. Reflectors consist of five pairs of alternating quarter-wavelength-thick SiO_2 and Ta_2O_5 layers. The cavity spacer is a Bi-substituted yttrium–iron-garnet layer, $Bi_{1.0}Y_2Fe_5O_x$. The spacer optical thickness is a half of wavelength. MMCs are grown on a glass substrate by the RF sputtering of corresponding targets in Ar^+ atmosphere with the sputtering pressure of 6 mTorr. Before fabrication of the top Bragg reflector, the sample is annealed in air at 700 °C for 20 minutes for the residual oxidation and crystallization of the Bi:YIG spacer. The MMC samples have $\lambda_{MC} \simeq 900$ nm and $\lambda_{MC} \simeq 1115$ nm that correspond to the Bi:YIG spacer thickness of approximately 195 nm and 245 nm, respectively. Hereafter λ_{MC} denotes the spectral position of the microcavity mode at normal incidence and determine the optical thickness of layers in MMC. For magnetophotonic crystals λ_{MC} is replaced by λ_{PC} which is related to the PBG center of the MPC at normal incidence.

The fabrication procedure [20] of 1D magnetophotonic crystals consists of successive rf-sputtering of SiO_2 and Bi:YIG from the corresponding targets in Ar^+ atmosphere with the residual pressure of 6 mTorr onto a 2.5 mm thick fused quartz substrate. The latter was initially optically polished with residual roughness below 5 nm to increase the interface quality of the MPC layers. Substrate temperature is kept at 140 °C at all sputtering stages to avoid the temperature-induced drift of the sputtering rate. After evaporation of each successive garnet layer, the MPC is removed from the sputtering machine and annealed in air at 700 °C for 20 minutes. The oxygen access during annealing is necessary for oxidation and crystallization of initially amorphous garnet films that are responsible for the ferrimagnetic state of MPC constituting garnet films.

Cleavage of MMCs and MPCs is studied using field-emission scanning electron microscope (FESEM). The FESEM images are shown in Fig. 8.1. Abrupt interfaces between magnetic garnet and dielectric layers as well as a reproducible layer thickness in all repeats can be seen. The layer-by-layer thickness deviation is estimated to be below 2 percents. The SiO_2 layers of the thickness of $d_1 \simeq (134 \pm 5)$ nm alternate the Bi:YIG layers of $d_2 \simeq (87 \pm 3)$ nm thick. The layers' thickness is kept constant

Fig. 8.1 The FESEM images of the MMC (*upper panel*) and MPC (*lower panel*) cleavages
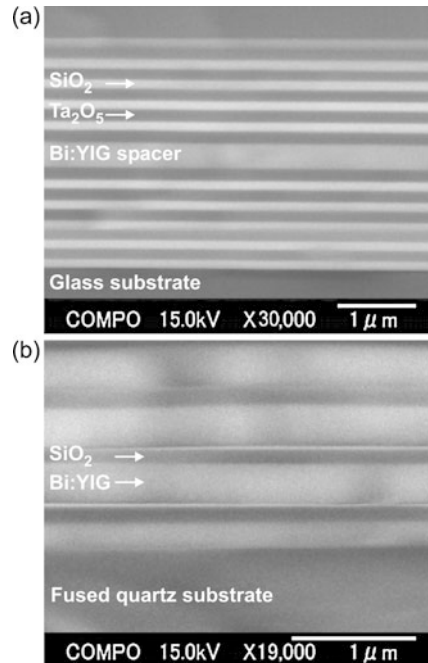

along the sample with the lateral corrugation in thickness being below 5 nm/μm. The atomic-force microscope (AFM) image of surface of the uppermost garnet layer of MPC showed that Bi:YIG layers are formed from columnar microcrystals with the lateral size ranging from 1 to 2 μm. The surface roughness is estimated to be approximately 2 nm everywhere at the garnet microcrystallite surface but at the boundaries where it is increased up to 5 nm.

Small gradual increase of the upper garnet layers thickness in MPCs is apparently associated with different shrinkage of garnet films during annealing and changes in sputtering rate due to the change of substrate temperature during sputtering. Hysteresis loops measured in vibrating sample magnetometer are shown in Fig. 8.2 and demonstrate that the coercivity of MPCs and MMCs is approximately 30 Oe for the longitudinal magnetic field. Saturating field which is slightly above 100 Oe indicates that the easy-magnetization axis is aligned along the Bi:YIG surfaces as expected for thin ferromagnetic films.

Spectroscopy of microcavities and one-dimensional photonic crystals implies the tuning the wave-vector component k_z parallel to the periodicity direction. Two configurations of the nonlinear spectroscopy are used in the study. In the first one, the fundamental radiation wavelength λ_ω is tuned at the fixed angle of incidence θ and is named below as spectroscopy in the frequency domain. The output of a nanosecond OPO laser system tunable from 720 nm to 1000 nm is used as the fundamental radiation. The laser energy is approximately 10 mJ per pulse, pulse width is below 2 ns and the laser spot area is below 0.5 mm^2.

Fig. 8.2 Magnetization curve
of a 1D-MPC
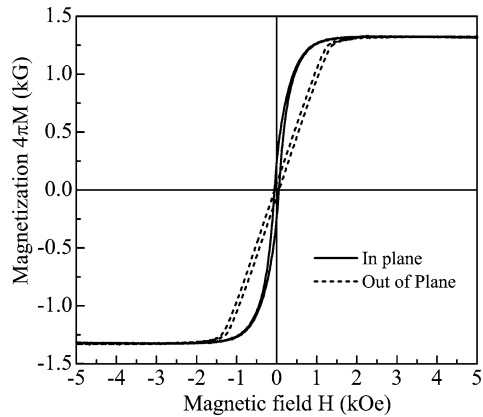
The case of the fixed fundamental radiation and tuning angle of incidence is named angular spectroscopy, or spectroscopy in the wave-vector domain. In that case, the output of a nanosecond YAG laser at the wavelength of 1064 nm is used. The energy of the fundamental beam is below 10 mJ per pulse, pulse width is approximately 15 ns and the laser spot area is about 1.0 mm^2. The radiation at the SH or TH wavelength is selected by an appropriate set of filters and detected by a photomultiplier tube. The SH intensity spectrum acquired in the frequency domain is normalized over the spectral sensitivity of the detection system and the tuning OPO curve using a SH intensity reference channel operating with a wedged z-cut quartz plate and with the detection system identical to the one in the sample channel.

The saturating *dc*-magnetic field of the strength up to 2 kOe providing the single-domain state is applied to the samples for the longitudinal and transversal NOMOKE, or along the normal to the samples for the polar NOMOKE using permanent FeNdB magnets. The schematic view of the experimental laser set-up along with the SHG interferometry scheme are shown in Fig. 8.3.

8.4 Optical and Magneto-Optical Spectra of Magnetophotonic Crystals and Microcavities

8.4.1 Faraday Effect Enhancement Induced by Multiple Interference

Figure 8.4 shows the transmission spectrum of MMC with $\lambda_{MC} \simeq 900$ nm. Low transmission is observed in the spectral region from 750 to 1000 nm, where the transmittance is decreased down to 10^{-3}. This corresponds to the photonic band gap of the structure. The PBG spectral width and the value of attenuation in the PBG are determined by the number of repeats and the refractive index difference in the SiO$_2$/Ta$_2$O$_5$ Bragg reflectors. A peak in the transmittance spectrum observed at
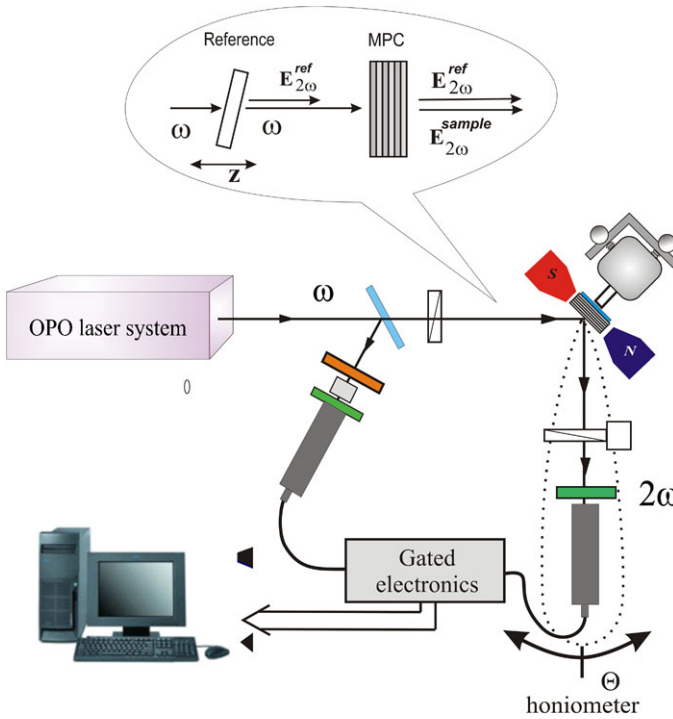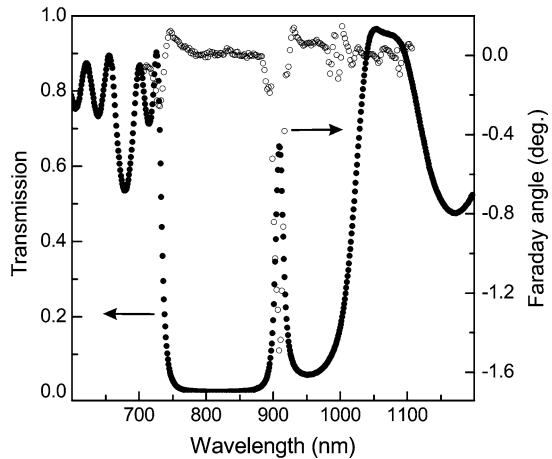
Fig. 8.3 Scheme of the experimental set-up for the SHG spectroscopy in magnetophotonic structures. Callout in the figure: the scheme of the SHG interferometry

Fig. 8.4 Spectra of transmittance (*filled circles*, *left scale*) and the Faraday rotation angle (*open circles*, *right scale*) of the MMC with $\lambda_{MC} \simeq 900$ nm measured at normal incidence

910 nm is attributed to the microcavity mode. The quality factor of MMC is $Q_{\omega} = \lambda_0/\Delta\lambda_0 \simeq 75$ where λ_0 is the resonant wavelength and $\Delta\lambda_0$ is the full width at half-magnitude. The spectrum of the Faraday rotation angle θ_F measured in crossed

Fig. 8.5 Spectra of
transmittance (*filled circles*,
left scale) and the Faraday
rotation angle (*open circles*,
right scale) of the MPC
measured at normal incidence
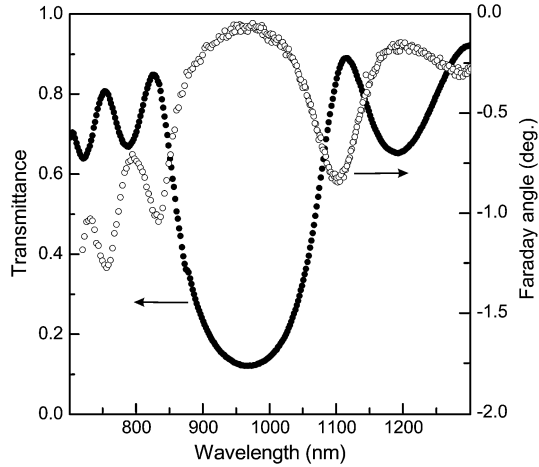
Glan-prizm polarizer and analyzer is also shown in Fig. 8.4. The θ_F spectrum has
a peak at the MMC mode, where θ_F is enhanced up to $-1.5°$. It corresponds to
an effective value of $-7.7°/\mu m$, which is approximately 50 times larger than the
Faraday rotation angle for a single Bi:YIG film of the same thickness deposited
directly on the substrate and measured at this wavelength.

Optical transmission spectrum of MPC is shown in Fig. 8.5. The spectral region
from 850 to 1100 nm with a small transmittance indicates the existence of photonic
band gap. The smallest transmittance value is reached at $\lambda_\omega \simeq 965$ nm and is ap-
proximately 0.10. Outside the PBG, optical spectrum demonstrates the interference
fringes, where transmittance is increased up to 0.9. θ_F is enhanced up to $-0.8°$ at
the long-wavelength edge of PBG at 1100 nm. It corresponds to an effective value
of $-0.75°/\mu m$, which is approximately 8 times larger than the Faraday rotation an-
gle for the single Bi:YIG film at this wavelength. For the wavelengths tuned inside
the PBG, Faraday rotation is strongly suppressed. The spectral position of the peaks
of θ_F at 750 nm and 830 nm correlate with the transmission spectrum maxima and
ride on the monotonous θ_F increase with the wavelength decrease associated with
the Faraday rotation spectrum of Bi:YIG.

The four-by-four matrix technique is utilized for the Faraday effect calculation.
The optical field inside each layer is given as a sum of four normal modes: right and
left circular polarized waves for both propagation directions. Then a set of four-by-
four matrices is calculated: each matrix corresponds to each layer of the structure
and determines the values of optical field on the layer boundaries. Multiplying all the
matrices one can obtain the matrix characterizing reflectance and transmittance of
the whole structure. Among the reflection and transmittance, Faraday angle and spa-
tial optical field distribution in the structure are calculated. The same approach can
be also applied for calculating the transversal Kerr effect spectra in 1D-MPCs [21].

For the calculation, the considered model of MMC consists of two Bragg reflec-
tors and a magnetic Bi:YIG MC layer squeezed between them. Each Bragg reflector
has five pairs of alternating $\lambda/4$-thick magnetic Bi:YIG and non-magnetic SiO_2 lay-
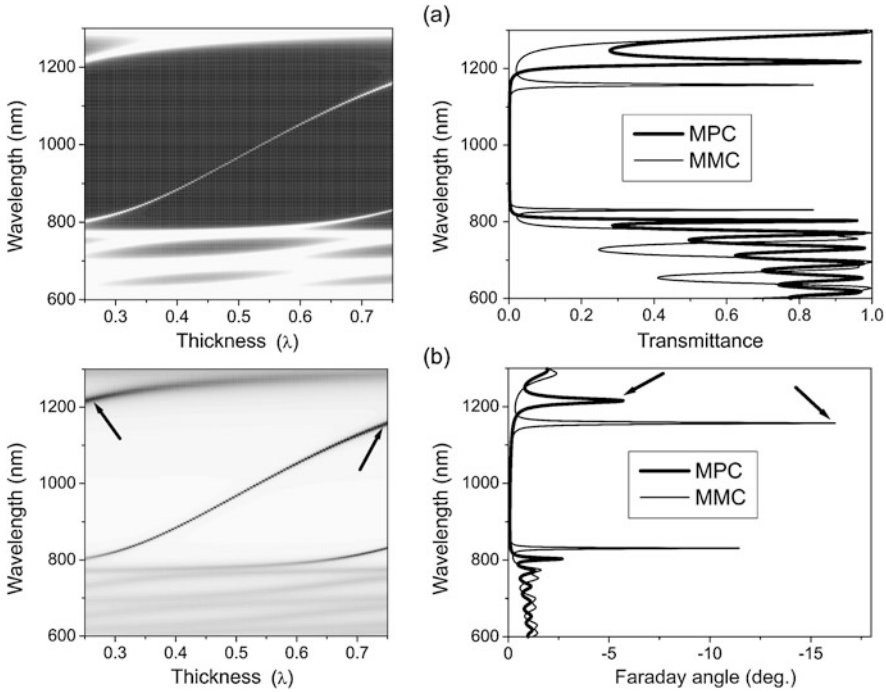
Fig. 8.6 Set of optical (**a**) and magneto-optical (**b**) spectra vs. thickness of the MMC cavity spacer. Transmittance and Faraday angle are shown by gray scale on the patterned plot. *Right plots* show the optical (**a**) and magneto-optical (**b**) spectra for MPC and $3\lambda/4$-MMC structures

ers. The refractive indices are supposed to be $n_{\mathrm{Bi:YIG}} = 2.6$ and $n_{\mathrm{SiO_2}} = 1.45$. The gyration vector is assumed to be $g_{\mathrm{Bi:YIG}} = 0.0054$ which is close to the experimental values. Optical thickness of the cavity spacer, Λ, is varied from $\lambda/4$ to $3\lambda/4$. The $\lambda/2$-thick cavity spacer corresponds to the MMC with the microcavity mode centered at the wavelength λ that coincides with the PBG center. The $\lambda/4$-thick spacer corresponds to the MPC with no microcavity mode. For $\Lambda = 3\lambda/4$, the microcavity mode is almost degenerated into a long-wavelength PBG edge, such a structure is called $3\lambda/4$-MMC. The transmittance (a) and Faraday angle (b) spectral dependences as functions of the spacer thickness are shown in Fig. 8.6 in the patterned plot. Right plots in Fig. 8.6 represent optical (a) and magneto-optical (b) spectra for MPC and $3\lambda/4$-MMC, labeled MPC and MMC, respectively.

White areas in the patterned plot in Fig. 8.6(a) correspond to the transmittance maxima. Black area in the patterned plot in Fig. 8.6(a) for the wavelengths from 800 to 1200 nm corresponds to the PBG, white curve across the PBG shows the thickness dependence of the microcavity mode, white areas at the PBG edges reveal the transmittance maxima. White area in the patterned plot in Fig. 8.6(b) shows a strong suppression of the Faraday effect at the wavelengths corresponding to the PBG. It can be seen that the Faraday angle θ_F is enhanced drastically at the microcavity mode. For $\Lambda = \lambda/4$ and $\Lambda = 3\lambda/4$, θ_F is enhanced at the PBG edges, especially at
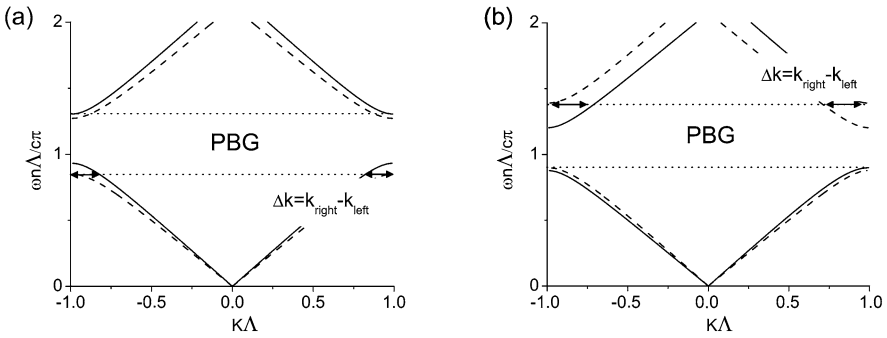
Fig. 8.7 (**a**) Band structures of 1D MPC for $\omega(\mathbf{k}_L)$ (*solid line*) and $\omega(\mathbf{k}_R)$ (*dashed line*) calculated for normal incidence at the 1D MPC consisted of layers of non-magnetic material with dielectric constant of $\varepsilon_1 = 2.1$ and magnetic one with diagonal component of dielectric constant of $\varepsilon_2 = 5.6$. (**b**) The same for $\varepsilon_1 = 5.6$ and $\varepsilon_2 = 2.1$

the long-wavelength one at 1200 and 1150 nm, respectively, as is indicated in the figure by black arrows.

The spectral positions of the Faraday rotation maxima are correlated with the transmittance maxima. The calculations show the absence of the ellipticity of the transmitted light polarization at the maximum of θ_F. It means that MPC and $3\lambda/4$-MMC give an opportunity to rotate efficiently the polarization plane without distortion and weakening the transmitted light. The θ_F enhancement in the $3\lambda/4$-MMC is nearly 3 times higher than the same in the MPC and reaches the values up to $-16°$ at the wavelength of 1150 nm corresponding to the long-wavelength PBG-edge.

8.4.2 Nonlinear Verdet Law in Magnetophotonic Crystals

The Faraday effect originates from different phase velocities for the right- and left-circular polarized waves traveling inside a magnetic medium. Taking into consideration the band structure of a photonic crystal, this approach can be extended on the Faraday effect in multilayered photonic structures. Figure 8.7 shows the dispersion relations $\omega(\mathbf{k}_L)$ and $\omega(\mathbf{k}_R)$ calculated for the left- and right-circularly polarized (RCP and LCP) optical waves propagating in MPC formed from a stack of magnetic and non-magnetic quarter-wavelength-thick layers. The main differences of dispersion properties for the normal modes and consequently for Faraday rotation are achieved at the photonic-band-gap edges. In the case of magnetic layers with higher refractive index, which corresponds to the experimental materials, Faraday effect is predicted at the long-wavelength PBG edge (Fig. 8.7(a)). In the opposite case (magnetic layers possess lower refractive index) short wavelength PBG edge exhibits an enhancement of the Faraday effect (Fig. 8.7(b)) [23].

It is worth mentioning that the difference in the dispersion properties and phase velocities of LCP and RCP waves in photonic crystals is accompanied by flattening
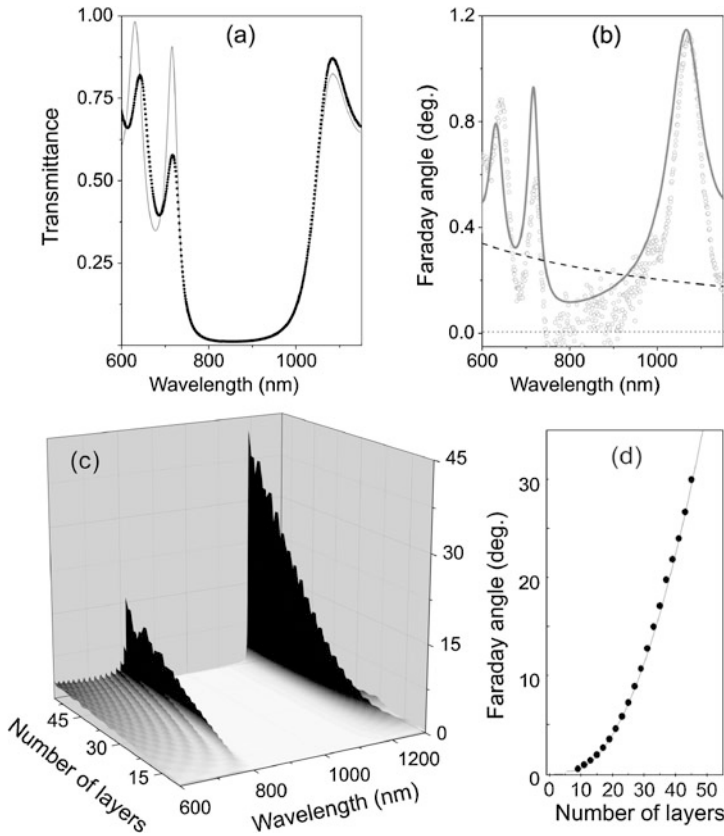
Fig. 8.8 (**a**) The transmission spectrum of 1D MPC upon normal incidence (*filled circles*) and its numerical approximation (*gray curve*). (**b**) Faraday rotation angle spectrum (*open circles*) and its numerical approximation (*gray curve*), dashed curve is the interference-subtracted spectrum of Faraday angle in homogeneous Bi:YIG slab of the same thickness. (**c**) Set of θ_F spectral dependencies vs. number of layers of MPC (3D plot) (numerical results). (**d**) Maximum θ_F vs. number of layers of MPC: calculated data and nonlinear fit

of the dispersion curves, resulting in the decrease of the group velocity of a wave packet traveling through the photonic crystal. It is equal to the localization of the electromagnetic field in different layers of MPC. A strong point lies in the fact that the difference in the phase velocities at different PBG edges is correlated with the optical field localization in magnetic and non-magnetic layers, correspondingly [22, 23].

Optical and magneto-optical spectra of 1D MPC are shown in Figs. 8.8(a) and (b). The spectral region from 725 to 1025 nm (where the transmission is strongly suppressed) corresponds to the photonic band gap of MPC. The Faraday rotation angle is also decreasing in this spectral region. Outside the PBG the transmission of the MPC increases and shows interference fringes. The Faraday rotation angle θ_F also oscillates with the spectrum having a local maxima at 640 and 720 nm, which cor-

relates well with the local transmission maxima. In can be seen that the largest enhancement of θ_F is observed near 1070 nm that coincides with the long-wavelength PBG edge.

The spectrum of the Faraday angle for a uniform slab of Bi:YIG with the thickness of 520 nm corresponding to the total Bi:YIG thickness in MPC is calculated using the known spectra of the diagonal and off-diagonal components of the complex dielectric function tensor of Bi:YIG with the same Bi concentration [19]. The θ_F enhancement coefficient at the long-wavelength PBG edge reaches the value of 6.5 in comparison with a homogeneous Bi:YIG slab, while θ_F increase at the short-wavelength PBG edge appears to be 1.9 and 2.7 at the certain interference fringes.

Both experimental spectra are fitted simultaneously using the four-by-four matrix technique with the spectral dependence of the refractive indices and absorption coefficients taken into account [19]. Particular applications of the 4×4 matrix formalism for 1D MPC are discussed in detail in Refs. [24, 25]. Briefly, transmission and polarization transformation of linearly polarized waves upon the propagation through 1D MPC is governed by a set of transfer matrices $\mathbf{M}_{ij}$ and Φ_j, accounting the boundary conditions for the complex amplitudes of the left- and right-circular polarized waves at the interface between ith and jth layers and their propagation through particular jth layer, respectively. Therefore, the field $\mathbf{E}_{N+1}$ outgoing from the 1D photonic crystal consisted of N layers is expressed for every wavelength λ as a result of tensorial multiplication of the incoming field $\mathbf{E}_0$ on series of transfer matrices:

$$\mathbf{E}_{N+1} = \mathbf{M}_{N+1,N}\Phi_N \cdots \mathbf{M}_{2,1}\Phi_1\mathbf{M}_{1,0}\mathbf{E}_0. \tag{8.11}$$

Vector-columns $\mathbf{E}_{N+1}$ and $\mathbf{E}_0$ are formed by a set of complex amplitudes $\mathbf{E}$ of normal modes, i.e. right- and left-circular polarized waves (indices r and l, respectively):

$$\mathbf{E}_0 = (1, r_r, 1, r_l)^T, \qquad \mathbf{E}_{N+1} = (t_r, 0, t_l, 0)^T, \tag{8.12}$$

where $r_{r,l}$ and $t_{r,l}$ are the amplitudes of the transmission and reflection coefficients for the two circular polarizations, which can be obtained by solution of a corresponding set of four algebraic equations. Optical properties of MPC are fully derived from $r_{r,l}$ and $t_{r,l}$; for example, the Faraday rotation angle is given by

$$\theta_F = \text{Im}\left[\arctan\left(\frac{t_r - t_l}{t_r + t_l}\right)\right], \tag{8.13}$$

while the real part of this expression characterizes the ellipticity η of transmitted light. In this way, reflection and transmission coefficients are given by

$$R = \left(|r_r + r_l|^2 + |r_r - r_l|^2\right)/4, \tag{8.14}$$

$$T = \left(|t_r + t_l|^2 + |t_r - t_l|^2\right)/4. \tag{8.15}$$

The enhancement is predicted and experimentally observed at the wavelength tuned at the long-wavelength PBG edge at 1060 nm. The Faraday effect is 6.5 times enhanced in comparison with single Bi:YIG layer with the thickness equal to the total thickness of the magnetic material in MPC. Experimental results are

in good agreement with theoretical calculations. The correlation of θ_F and transmittance maxima opens up prospects for practical application of MPC in various magneto-optical devices as it gives an opportunity to rotate polarization plane without neither distortion nor weakening transmitted light. The calculations also show that ellipticity of the transmitted light η achieves a minimum at the maximum of θ_F.

An increase of the number of layers in MPC, N, leads to a better field localization in MPC combined with the total magnetic material thickness increase. Such combination is expected to result into specific thickness dependence $\theta_F(N)$. Figure 8.8(c) shows a 3D-plot of thickness and spectral dependence $\theta_F(\lambda, N)$. Faraday angle maxima are achieved at both PBG edges. However, for considered experimental situation as magnetic layers have larger refractive index, θ_F enhancement at the long-wavelength PBG edge is significantly larger than that at the short-wavelength edge and shows a *nonlinear* dependence $\theta_F(N)$ of maximum values achieved at the wavelength tuned at the PBG edge (Fig. 8.8(d)). It can be interpreted as Verdet rule violation. As has been mentioned above for the uniform media $\theta_F(D) \sim D$, where D is magnetic material thickness. However, in the case of multilayered structure this rule is broken, MPC exhibits *nonlinear* $\theta_F(D) \sim D^2$ dependence. In conclusion combination of spatial optical field distribution with difference in phase velocities of RCP in LCP is shown to be responsible for nonlinear dependence of $\theta_F(D) \sim D^2$.

Spectral dependences of spatial optical field distribution in the sample for the $\lambda/4$-MPC (a) and the $3\lambda/4$-MMC (b) are given in Fig. 8.9. In the case of the $\lambda/4$-MPC, the field is localized in all magnetic layers at the long-wavelength PBG edge at approximately 1200 nm and the field amplitude in the central layer is 2.7 times higher than that of the incident light. The $3\lambda/4$-MMC provides the better field localization in all magnetic layers in comparison with the $\lambda/4$-MPC, the field amplitude in the microcavity spacer at the wavelength of 1150 nm is almost two times higher than that in the $\lambda/4$-MPC sample. The field localization in magnetic layers indicates the constructive interference resulted in the Faraday effect enhancement and vividly explains the Θ_F enhancement at the PBG edge of $\lambda/4$-MPC and $3\lambda/4$-MMC.

The increase of number of layers in MPC leads to the enhancement of Faraday rotation at the PBG edge by the combined effect of field localization and the increase of magnetic material thickness. The enhancement up to $\theta_F = 45°$ is expected in $3\lambda/4$-MMC consisting of about 20 pairs of layers. Therefore, Faraday rotation angle in the finite MPCs appears to be a nonlinear function of the total thickness of magnetic material in the stack that can be interpreted as the nonlinear Verdet law. Relation between the enhancement of the Faraday rotation and localization of optical field in magnetic layers is treated as a Borrmann-type effect. This relation shows that the Faraday rotation can be considered as a measure of the density of photonic states trapped within Bi:YIG layers [22, 23].
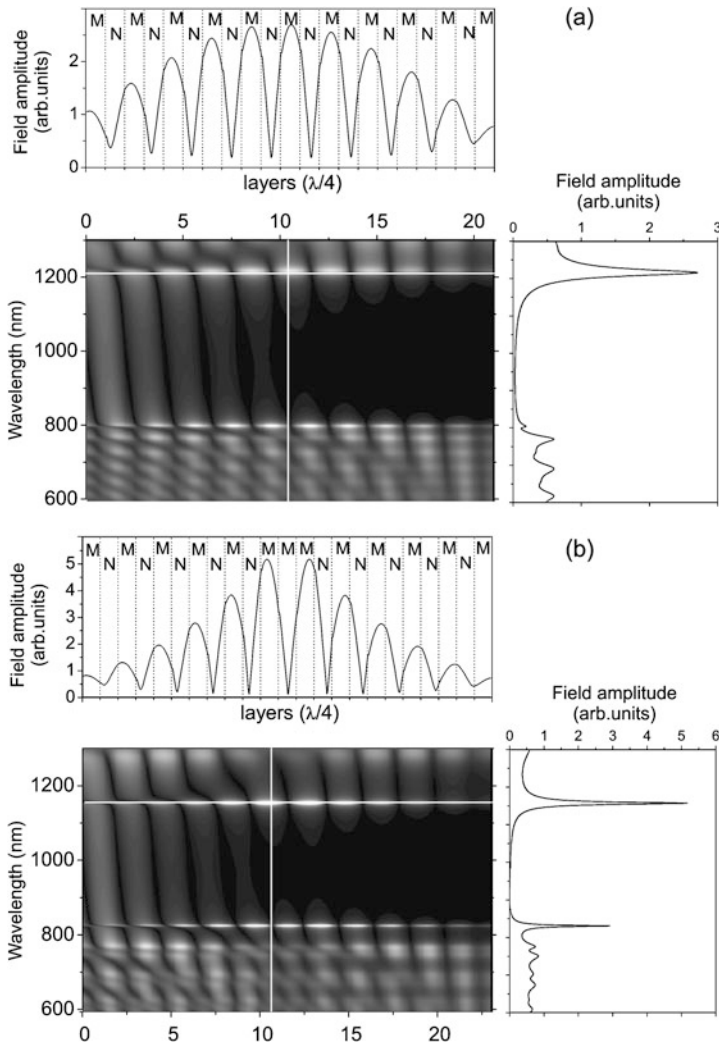
Fig. 8.9 Spectral dependence of spatial optical field distribution in $\lambda/4$-MPC (**a**) and $3\lambda/4$-MMC (**b**). Field amplitude is shown by gray scale on the patterned plot. White color corresponds to the maxima of the field amplitude. *Upper* and *right plots* at each panel represent spatial field distribution at the PBG edge and its spectrum in the central layer taken at cross sections marked by *white lines*. Magnetic layers are labeled M and non-magnetic layers N

8.5 MSHG and MTHG in Magnetophotonic Microcavities and Magnetophotonic Crystals

In this section, the results of the nonlinear magneto-optical Kerr effect in magnetic microcavities formed from dielectric Bragg reflectors and a magnetic garnet spacer are discussed [26, 28–30, 35, 36]. Magnetization-induced variation of the

Fig. 8.10 Transversal
NOMOKE in SHG measured
in the *p*-in, *p*-out polarization
combination for opposite
directions of magnetic field,
solid, and open circles,
respectively. *Inset*: the
spectrum of the SHG
magnetic contrast in the
vicinity of the microcavity
mode
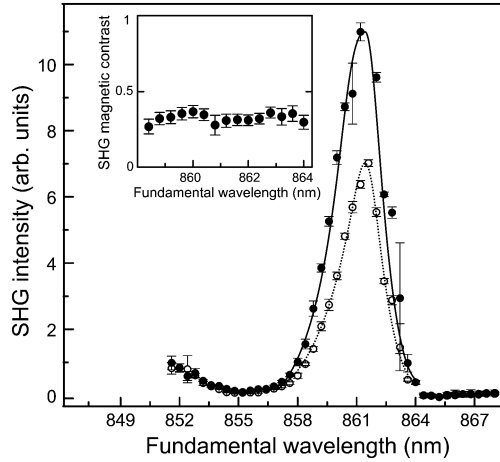
SH intensity, rotation of the SH wave polarization, and the shift of the relative SH phase are observed at the wavelength (angular) resonance of the fundamental radiation with the microcavity mode. The symmetry properties of quadratic susceptibility (pseudo)tensors allow the clear separation of the magneto-optical effects. Namely, magnetization-induced changes in the SH intensity and relative phase are observed in the transversal configuration, while the SH wave polarization rotation is obtained in the longitudinal and polar configurations. Then, the mechanisms of magnetization-induced variations in SH intensity in MPCs consisted of the stack of Bi:YIG layers are discussed in terms of local field enhancement phase-matching fulfillment [36]. Finally, the MTHG studies in magnetophotonic microcavities are reviewed [36].

8.5.1 Transversal NOMOKE in MSHG: Intensity and Phase Effects

Intensity effects in MSHG are demonstrated in Fig. 8.10 where the spectral dependence of the SH intensity measured in the MMC with $\lambda_{MC} \simeq 900$ nm is shown [26, 36]. Dc-magnetic field is applied in the transversal configuration, i.e. $\mathbf{M} = (0, M_Y, 0)$.

The SH intensity is enhanced as the fundamental wave is tuned across the microcavity mode. The ratio of the intensities for the opposite directions of the magnetic field is almost two. Spectral dependence of the magnetic contrast in the SH intensity, $\rho = (I_+ - I_-)/(I_+ + I_-)$, where $+$ and $-$ denote the directions of the field, is shown in the inset of Fig. 8.10. ρ reached values of 0.3 and appears to be independent of spectrum. The inverting the magnetic-field direction varies only the SH intensity and no spectral shifts of SHG resonances are observed.

Another experimental configuration is angular spectroscopy. Figure 8.11 shows the SH intensity as a function of the angle of incidence measured in the MMC with

Fig. 8.11 Transversal
NOMOKE in SHG measured
in the *p*-in, *p*-out polarization
combination for opposite
directions of magnetic field,
solid, and open circles,
respectively. *Inset*: the
angular spectrum of the SHG
magnetic contrast in the
vicinity of the microcavity
mode
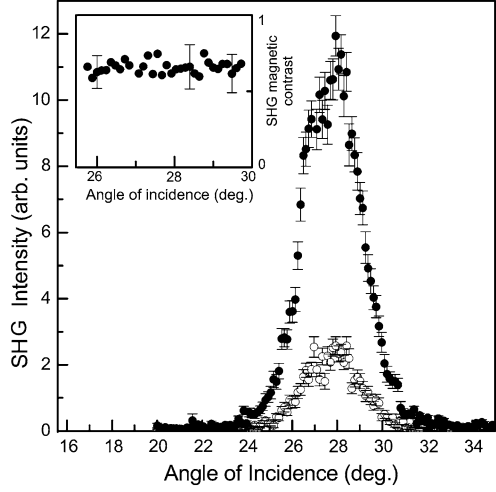
$\lambda_{MC} \simeq 1115$ nm in the transversal NOMOKE configuration. The inverting the magnetic field direction varies $I_{2\omega}$ approximately by a factor of four. The angular spectrum of the SHG magnetic contrast shown in the inset of Fig. 8.11 is independent of the angle of incidence and achieves values of 0.65.

Magnetization-induced changes of the relative phase of the SH wave are observed using SHG interferometry [27]. The SHG interference patterns are obtained by translating the SHG reference sample along the direction of the laser beam propagation, so that the distance l between the reference and the MMC sample is varied. The SHG reference sample is a 30 nm-thick indium tin oxide film deposited on fused quartz plate. The total SH intensity, $I_{2\omega}(l, \mathbf{M})$, is produced by the coherent sum of the SH waves from the reference, $\mathbf{E}_{2\omega}^r$, and the MMC sample, $\mathbf{E}_{2\omega}(\mathbf{M})$:

$$I_{2\omega}(l, \mathbf{M}) = \frac{c}{8\pi} \left| \mathbf{E}_{2\omega}^r(l) + \mathbf{E}_{2\omega}(\mathbf{M}) \right|^2$$

$$= I_{2\omega}^r + I_{2\omega}(\mathbf{M}) + 2\alpha \sqrt{I_{2\omega}^r I_{2\omega}(\mathbf{M})} \cos\left(2\pi kl + \Phi_{rs}(\mathbf{M})\right), \quad (8.16)$$

where $k = 2\Delta n/\lambda_\omega$ with $\Delta n = n_{2\omega} - n_\omega$ describing air dispersion, Φ_{rs} is the phase difference between the reference and sample SH waves, and $\alpha < 1$ is the phenomenological parameter accounting for both spatial and temporal coherence of the laser pulses. Changing the magnetic field direction to the opposite one shifts the SHG interference patterns by almost a half of a period. This indicates the shift of the relative SH phase at approximately 180°. The angular dependence of the SH phase shifts measured at the vicinity of the mode is shown in Fig. 8.12. The phase shifts are slightly smaller than 180° and almost constant in θ.

The SH intensity variations which are odd in the magnetization are observed only in the transversal NOMOKE configuration. In the *p*-in, *p*-out polarization combination, the non-magnetic (crystallographic) SH field E^{NM} is induced by χ_{zzz}, χ_{zxx}, and χ_{xxz} elements of the $\chi^{(2,0)}$ tensor. The magnetization-induced SH field

Fig. 8.12 Phase effects in MSHG: The magnetization-induced shift of the relative SH phase measured in the transversal NOMOKE configuration in the angular vicinity of the microcavity mode. *Inset*: row SHG interference patterns for opposite directions of magnetic field measured at $\theta = 28°$
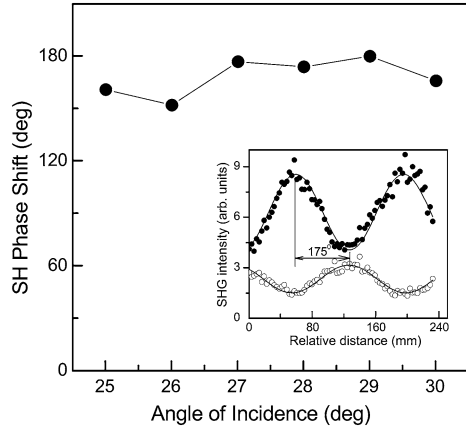
$E^{\mathrm{M}}\exp(i\varphi_M)$ is generated by χ_{xzzY}, χ_{zxzY}, and χ_{xxxY} elements of the $\chi^{(2,1)}$ tensor and is shifted in phase by φ_M with respect to the E^{NM} field. Interference of the non-magnetic and magnetization-induced SH fields leads to the cross-term $\pm 2E^{\mathrm{NM}}E^{\mathrm{M}}\cos\varphi_M$ in the SH intensity. This term changes the sign upon the reversing the magnetic-field direction and results in the SH intensity variations, which are linear in **M**. The relative value of these variations depends on the phase shift φ_M. The constant value of ρ in the vicinity of the microcavity mode indicates that the SH fields E^{NM} and E^{M} are enhanced similarly due to the fundamental field localization. For the 1064-nm fundamental wavelength φ_M takes the values close to $0°$ or to $180°$ for opposite directions of **M**. This is seen in phase measurements, where the magnetization-induced shift of the relative SH phase is close to $180°$. For small refraction angle θ_ω in the Bi:YIG layer and $\varphi_M \simeq 0$, the ratio between E^{NM} and E^{M} can be estimated as

$$E^{\mathrm{NM}}/E^{\mathrm{M}} \simeq \chi_{xxxY} M_Y / (2\chi_{zxx}\tan\theta_\omega). \tag{8.17}$$

It gives the ratio of $\chi_{xxxY} M_Y / \chi_{zxx} \simeq 0.15$ for $\rho \simeq 0.65$.

8.5.2 Longitudinal and Polar NOMOKE in MSHG: Polarization Effects

Figure 8.13 shows dependences of the SH intensity on the orientation angle Θ of the analyzer axis measured for opposite directions of magnetic field applied in the longitudinal NOMOKE configuration [28, 30]. The fundamental radiation is *s*-polarized and its wavelength is 868 nm, which corresponds to the microcavity mode. The SH wave is linearly polarized. The longitudinal NOMOKE manifests itself in the magnetization-induced rotation of the SH wave polarization. The angle of polarization rotation is $\Delta\Theta = 38°$ for the angle of incidence of $30°$ and almost $\Delta\Theta = 48°$ as the angle of incidence is $15°$.
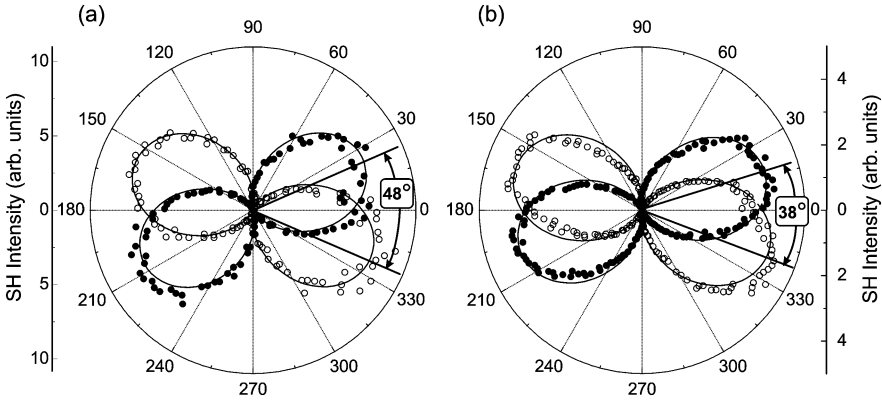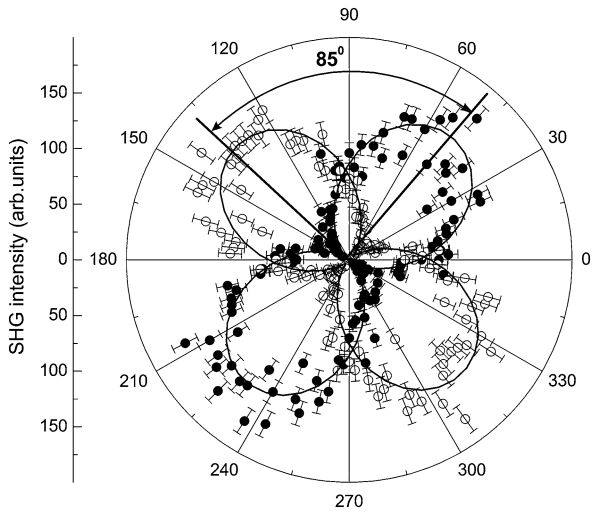
Fig. 8.13 SH wave polarization diagrams measured for opposite directions of magnetic field applied in the longitudinal configuration to the MMC with $\lambda_{MC} \simeq 900$ nm. The angle of incidence is 15° (**a**) or 30° (**b**). The zeroth value of the analyzer angle corresponds to the p-polarized SH wave. *Curves* are the fit to intensity of the linearly polarized wave

Fig. 8.14 SH wave polarization diagrams measured in MMC with $\lambda_{MC} \simeq 1115$ nm for the opposite directions of the magnetic field applied in the longitudinal configuration. The angle of incidence is 28°. The zeroth value of the analyzer angle corresponds to the p-polarized SH wave. *Curves* are the fit to intensity of the linearly polarized wave

The magnetization-induced rotation of the SH wave polarization plane is increased as the fundamental radiation is tuned to the long-wavelength region. Figure 8.14 shows the SH wave polarization diagrams measured for the s-polarized fundamental radiation with $\lambda_\omega = 1064$ nm. The magnetization-induced rotation of the polarization plane up to $\Delta\Theta = 85°$ is observed, while for the p-polarized fundamental radiation the $\Delta\Theta$ value is approximately 60°.

In the longitudinal NOMOKE configuration, the non-magnetic and magnetization-induced SH fields are polarized orthogonally, E^{NM} being p-polarized and E^M—s-polarized, respectively. The magnetization-induced effects appear in rota-

Fig. 8.15 Polarization effects in MSHG: The spectrum of the SH wave polarization rotation in MMC with $\lambda_{\mathrm{MC}} \simeq 900$ nm upon the inverting the magnetic field direction in the polar NOMOKE configuration
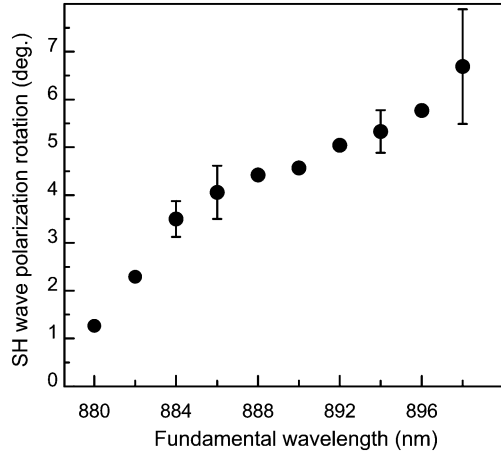
tion of the polarization plane of the total SH light. The SH intensity depends on the analyzer angle Θ as

$$I_{2\omega}(\Theta) \propto \left| E_p^{\mathrm{NM}} \cos\Theta + E_s^{\mathrm{M}} \exp(i\phi_M) \sin\Theta \right|^2, \tag{8.18}$$

where the phase shift ϕ_M describes the SH field ellipticity and the subscripts s and p indicate the polarization of the corresponding SH fields. The SH wave is considered as linearly polarized with $\phi_M \simeq 0$. The rotation angle of the SH field polarization upon the inverting the magnetic field direction is estimated as $\Delta\Theta \simeq 2\arctan(E_s^{\mathrm{M}}/E_p^{\mathrm{NM}})$ and depends on the ratio of corresponding elements of the $\chi^{(2,0)}$ and $\chi^{(2,1)}$ tensors [28]. For longitudinal NOMOKE configuration and the s-polarized fundamental radiation

$$\Delta\Theta \simeq 2\arctan\left(\chi_{yyyX} M_X / (\chi_{zyy} \sin\theta_\omega)\right). \tag{8.19}$$

For $\Delta\Theta_{2\omega} = 48°$ and $\theta = 15°$, it gives the ratio of $\chi_{yyyX} M_X/\chi_{zyy} \simeq 0.1$ at $\lambda_\omega = 870$ nm, which is close to the value of the $\chi_{xxxY} M_Y/\chi_{zxx}$ ratio estimated from the transversal NOMOKE measurements. For $\Delta\Theta_{2\omega} = 85°$, $\theta = 28°$, it gives the ratio of $\chi_{yyyX} M_X/\chi_{zyy} \simeq 0.15$ at $\lambda_\omega = 1064$ nm.

The spectrum of the polar NOMOKE is shown in Fig. 8.15. Tuning the fundamental wavelength through the microcavity mode leads to a gradual increase of $\Delta\Theta$, from 1° to 7°. In the polar NOMOKE configuration, E_s^{M} is yielded by three sources. First, it is generation of the s-polarized magnetization-induced SH field described by the χ_{yxzZ} element, $E_{s,1}^{\mathrm{M}} = F_y^{2\omega} F_x^\omega F_z^\omega \chi_{yxzZ} M_Z I_\omega^2$ with F_i^Ω is the Green-function correction for corresponding component of the SH or fundamental wave amplitudes [31] and I_ω is the fundamental wave intensity. Second, it is the generation of the s-polarized SH field via the χ_{yzy} element of the crystallographic quadratic susceptibility, $E_{s,2}^{\mathrm{M}} = F_y^{2\omega} F_z^\omega F_y^\omega \chi_{yzy} I_\omega^2 \sin(\Theta_\omega/2)$, where Θ_ω is the linear (Faraday) rotation angle of the fundamental wave. The Faraday rotation of the fundamental radiation is greatly enhanced at the resonance with the microcavity mode due to multiple reflection in the Bi:YIG spacer [32] that is the directly attributed to the

Fig. 8.16 Angular spectra of the THG intensity for different polarization combinations of the pump and THG modes
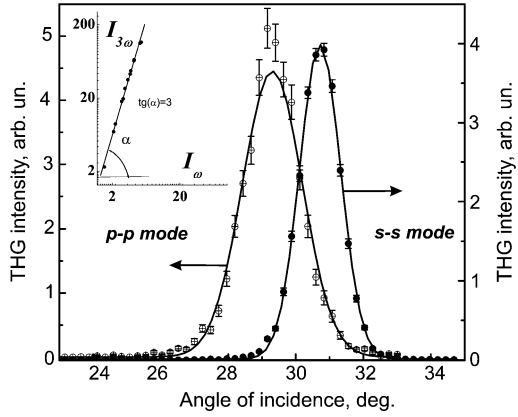
nonreciprocity of the light propagation in the magnetic materials. Faraday rotation of initially p-polarized fundamental wave is equivalent to the appearance of the s-polarized component of the fundamental radiation that allows generation of the s-polarized SH wave in the m-in, s-out polarization combination. The last source of the s-polarized SH wave is the Faraday rotation of the p-polarized SH wave, $E_{s,3}^{\mathrm{M}} = E_p^{\mathrm{NM}} \sin(\Theta_{2\omega}/2)$, where $\Theta_{2\omega}$ is the Faraday rotation angle of the SH wave. For small angles of incidence, the contribution of the χ_{zzz} susceptibility element is small and $E_p^{\mathrm{NM}} = (F_z^{2\omega}(F_x^\omega)^2 \chi_{zxx} + F_x^{2\omega} F_z^\omega F_x^\omega \chi_{xzx}) I_\omega^2$. For the correct calculation of the total SH wave polarization rotation, $\tan \Delta \Theta = 2(E_{s,1}^{\mathrm{M}} + E_{s,2}^{\mathrm{M}} + E_{s,3}^{\mathrm{M}})/E_p^{\mathrm{NM}}$, one should know the relation between χ_{yzy}, χ_{zxx} and χ_{xzx} elements. However, for the estimation, suppose them to be equal one to each other. For small refractive angles θ_ω, Green-function corrections $F_z^{2\omega}, F_z^\omega \to 0$ and $F_x^{2\omega}, F_x^\omega, F_y^\omega, F_y^{2\omega} \to 1$, $\tan \Delta \Theta \simeq \Delta \Theta$, $\sin \Theta_{2\omega} \simeq \Theta_{2\omega}$ and $\sin \Theta_\omega \simeq \Theta_\omega$. The $\Delta \Theta$ value can be estimated within these assumptions as [35]

$$\Delta \Theta \simeq \chi_{yxzZ} M_Z / \chi_{zxx} + \Theta_\omega/2 + \Theta_{2\omega}. \tag{8.20}$$

The first term in (8.20) is wavelength-independent since the elements of the $\chi^{(2,0)}$ and $\chi^{(2,1)}$ tensors are constant within narrow spectral region of the MC mode. The term $\Theta_{2\omega}$ is also independent from λ_ω due to large absorption at the SH wavelength. The second term in (8.20), $\Theta_\omega(\lambda_\omega)$ reaches the maximum for oblique angles of incidence when s- and p-modes are overlapped. Note that the rotation of the SH field polarization plane via *non-magnetic* quadratic susceptibility is related strongly to the symmetry of the magnetic spacer since it requires the non-zero χ_{yzy} element.

8.5.3 MTHG in Magnetophotonic Microcavities

Optical third harmonic generation in MMC was first studied in the absence of the external magnetic field in near-resonant conditions for the excitation of the microcavity mode. Figure 8.16 shows the angular spectra of the THG intensity for different polarization combinations of the pump and THG modes. In accordance with

Fig. 8.17 Intensity effects in MTHG: Angular spectra of transversal NOMOKE in THG measured in MMC with $\lambda_{MC} \simeq 1115$ nm for opposite directions of magnetic field, *solid*, and *open circles*, respectively. *Squares* shows the THG magnetic contrast in the angular vicinity of the microcavity mode
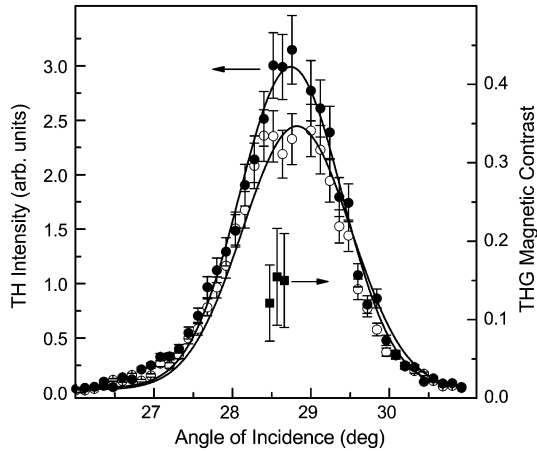

the symmetry analysis summarized in Table 8.1, only *s*-in, *s*-out and *p*-in, *p*-out geometries are allowed for the THG in an isotropic medium that was proven experimentally. The magnetization-induced effects in the intensity of the third-harmonic generation are studied for the transversal NOMOKE configuration. The symmetry analysis shows that for this geometry of the magnetic field application the elements of the cubic susceptibility tensor $\chi^{(3,1)}$, which are odd in the magnetization, lead to the appearance of additional contributions to the *p*-polarized THG signal. The experiments performed for the *p*-in, *p*-out polarization combination for the transversal NOMOKE do not reveal magnetization-induced variations of the THG intensity within the experimental accuracy, on the contrary to a much larger magnetic contrast in the SHG intensity.

In order to reveal a small magnetization-induced effect in the THG intensity, the following experimental scheme is chosen. The *p*-polarized THG intensity is measured, while the polarization plane of the fundamental radiation is chosen to form an angle of about 5–10 degrees out from the *s*-polarization. For this polarization combination, almost the entire magnetic component of the THG intensity generated by the $\chi_{zyyy}X$ component is recorded, which interfered with a strongly suppressed non-magnetic *p*-in, *p*-out THG signal. Figure 8.17 shows the THG spectra measured in the wave-vector domain for the oppositely directed magnetic field for the transversal NOMOKE configuration. Similar to the magnetization-induced SHG, the THG magnetic contrast is determined by the expression $\rho_{3\omega} = (I_+^{3\omega} - I_-^{3\omega})/(I_+^{3\omega} + I_-^{3\omega})$, where $I_+^{3\omega}$ and $I_-^{3\omega}$ are the THG intensities for the oppositely directed magnetic fields. The measured value of the magnetic contrast in the THG intensity is found to be about 0.1 for the angles of incidence corresponding to the resonance with the microcavity mode.

The observed THG magnetic contrast is due to the third-order susceptibility $\chi^{(3,1)}$ components' interference with the non-magnetic ones due to the internal homodyne effect. This results in the revelation of a weak magnetic THG contribution on the background of a much stronger non-magnetic THG. In this case, an esti-

Fig. 8.18 *Filled circles.* Intensity spectrum of the SH wave reflected from MPC in the *p*-in, *s*-out polarization combination in longitudinal configuration of the dc-magnetic field application. *Line*: the Faraday rotation spectrum at normal incidence
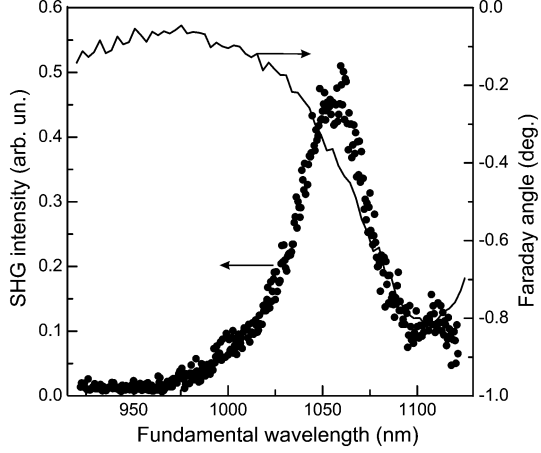

mation can be made for the χ_{zyyyX} element as $\chi_{zyyyX} \sim 10^{-3}\chi_{\text{eff}}^{(3)}$, where $\chi_{\text{eff}}^{(3)}$ is the effective non-magnetic cubic susceptibility responsible for the generation of the *p*-polarized TH field with *s*- or mixed-polarized fundamental radiation.

8.5.4 Phase-Matched MSHG in Magnetophotonic Crystals

Figure 8.18 shows the spectrum of the SH intensity measured in MPC for the *p*-in, *s*-out polarization combination in the longitudinal NOMOKE configuration. Spectrum demonstrates the resonant enhancement at $\lambda_\omega \simeq 1055$ nm. The spectral position of the peak correlates with the long-wavelength PBG edge, which is blue-shifted from 1110 nm for oblique angles of incidence. In the *p*-in, *s*-out polarization combination, the non-magnetic (crystallographic) SH field $E_{2\omega}^{\text{NM}}$ induced by the $\chi^{(2,0)}$ tensor is equal to zero. Thus in the longitudinal NOMOKE configuration as $\mathbf{M} = (M_X, 0, 0)$, the SH intensity is entirely associated with the magnetization-induced SH field $E_{2\omega}^{\text{M}}$ induced by the χ_{yxxX} and χ_{yzzX} elements of the $\chi^{(2,1)}$ tensor. The MSHG enhancement in MPC is interpreted as a result of the phase matching conditions achieved as the fundamental wavelength is tuned across the PBG edge. This stems from the comparison of the amplitudes of the SHG resonances at PBG edges. The intensity enhancement at the long-wavelength PBG edge of MPC is at least five times larger than that at the short-wavelength edge. Spatial localization of the optical field is similar at both PBG edges and the SHG enhancement yielded by this mechanism is expected to be the same order of magnitude. Inversion of the magnetic field direction does not change the value of the SH intensity, which indicates that $E_{2\omega}^{\text{NM}} = 0$.

This is in contrast to the *p*-in, *p*-out polarization combination. In the transversal NOMOKE configuration the non-magnetic SH field $E_{2\omega}^{\text{NM}}$ interferes with the magnetization-induced SH field $E_{2\omega}^{\text{M}} \exp(i\varphi_M)$. The intensity cross-term

Fig. 8.19 The SHG spectra of MPC in the *p*-in, *p*-out polarization combination and in transversal magnetic-field configuration measured for opposite directions of the dc-magnetic field; *open* and *filled circles*, respectively. *Line*: the Faraday rotation spectrum at normal incidence
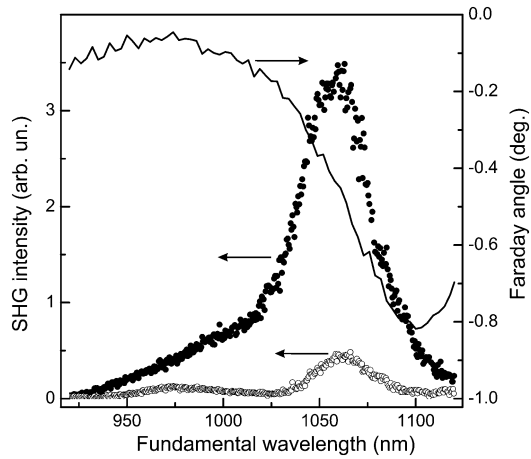
$\pm 2E_{2\omega}^{\mathrm{NM}} E_{2\omega}^{\mathrm{M}} \cos\varphi_M$ changes the sign upon changing the magnetic field direction and manifests the internal homodyne effect in MSHG. This term leads to variations of the SH intensity, which are linear in $\mathbf{M}$ and depends on the relative phase φ_M between $E_{2\omega}^{\mathrm{NM}}$ and $E_{2\omega}^{\mathrm{M}}$. Figure 8.19 shows the SHG spectra measured for opposite directions of magnetic field in the transversal NOMOKE configuration. The SHG intensity is many-fold enhanced in the spectral vicinity of 1050 nm corresponding to the phase-matched conditions for SHG at the long-wavelength PBG edge of MPC. Changing the magnetic field direction varies the SH intensity approximately by a factor of seven at $\lambda_\omega \simeq 1055$ nm that indicates the noticeable interference between the $E_{2\omega}^{\mathrm{NM}}$ and $E_{2\omega}^{\mathrm{M}}$ fields. At $\lambda_\omega \simeq 1025$ nm the SH intensity for one of the magnetic field direction is close to zero. It means that the contrast of the magnetization-induced variations in the SH intensity is close to unit, which the upper limit for SHG magnetic contrast.

8.5.5 Nonlinear Magneto-Optical Kerr Effect in Three-Dimensional Magnetophotonic Crystals

As has been discussed above MPC and MPMC are attractive structures for potential applications. One of the perspective approaches for the composition of MPC is the infiltration of a magnetic material into porous PC template, thus the structure periodicity is governed by the non-magnetic porous PC and the magneto-optical properties are supplied by the infiltrated magnetic material.

Synthetic opals composed of spheres of silica oxide are unique self-assembling materials that form a strongly periodic 3D structure. Depending on the size of the constituting spheres they can reveal the PBG in the visible and near infra-red spectral regions. The structure of the opals supposes the existence of hexagonal system of pores with the volume fraction of no less than 26 % (in case of close packed

Fig. 8.20 SEM image of the experimental opal sample
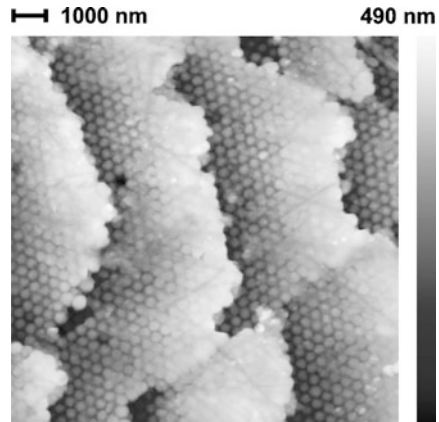
silica oxide spheres). As concerning 3D MPCs, there are several papers related to studies of their magnetic and structural properties, including the observation of an enlarged Faraday rotation [10, 11]. Here we describe the results on the composition and investigation of the nonlinear magneto-optical Kerr effect (NOMOKE) in 3D MPC based on artificial opals infiltrated by yttrium–iron garnet (YIG). Here we will mainly describe the results from [37].

8.5.5.1 Sample Composition and Characterization

Templates of artificial opals were composed of monodisperse amorphous close-packed SiO_2 spheres with the diameter of about 330 nm. The bare opals have been grown by use of the technological route described in [39]. The samples studied in the nonlinear-optical experiments were the plates of about $(4 \times 4 \times 0.5)$ mm in size cut parallel to the (111) opal crystalline plane (Fig. 8.20). Opal templates possessed polydomain structure, the size of a single domain with highly ordered SiO_2 spheres ranged from 30 to 100 μm.

Two technological approaches were used for the infiltration of opals templates by yttrium–iron garnet. The first batch of samples was soaked by the colloidal solution of yttrium–iron hydroxides taken in stoichiometric proportion, the size of the colloidal particles being about 5 nm. The filling factor of pores was 25–30 % vol. In order to form YIG nanocrystals inside the pores the subsequent annealing at 1300 K was performed. X-ray diffraction analysis has shown the appearance of the strongest YIG peak from [420] set of planes. Such a relatively poor XRD spectrum can evidently be caused by the formation of silicate due to the reaction of yttrium oxide with SiO_2, so that only a small amount of crystalline YIG was formed.

An attempt to prevent the chemical reactions between the yttrium oxide and the silica matrix was made for the second set of samples, where a thin platinum layer covering the inner surface of the opal matrix was deposited prior to the infiltration by YIG. A thin layer of platinum (2–3 nm) is deposited on silica surface using the

Fig. 8.21 Magnetization
curve for opal-Pt-YIG
composite PC
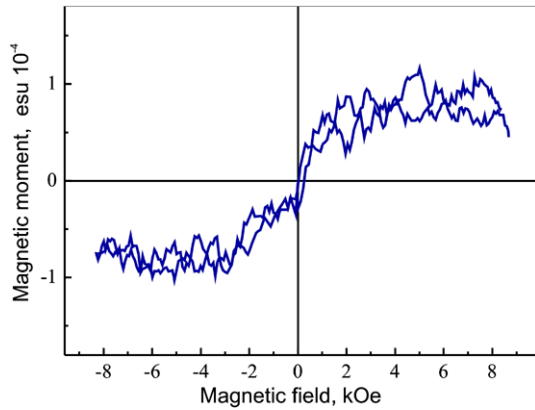
method described in [17, 18]. The gravimetric measurements have shown that the filling factor of pores by Pt is about 5 % vol. After the deposition of a thin Pt layer the samples were infiltrated by an aqueous solution of yttrium and iron acetates followed by the thermal annealing in a similar way as described above for bare opals. The filling factor of pores with YIG was about 30 % vol. In the case of this set of samples the XRD analysis revealed the existence of the following crystalline phases: Pt, yttrium–iron garnet $Y_3Fe_5O_{12}$ with the lattice parameter $a = 12.25(7)$ Å, as well as some impurities [γ-Fe_2O_3, yttrium silicates and crystalline forms of SiO_2 (cristobalite and tridymite)]. Before starting the optical measurements, the rest volume of pores in the opal-YIG and opal-Pt-YIG samples was infiltrated with glycerol to decrease diffuse scattering. Magnetization measurements for Pt-covered YIG-infiltrated opals (Fig. 8.21) have shown that within the experimental accuracy there is no hysteresis in the magnetization curve, while for the magnetic fields over approximately 2 kOe the magnetization is close to the saturation. Such features are typical for super-paramagnetic systems composed of nanocrystallites of magnetic materials such as YIG crystallized within opals' nanopores.

Optical characterization of YIG-infiltrated opals was first performed by linear reflectance spectroscopy. The reflectance spectra measured for different angles of incidence of the fundamental beam with the wavelength range from 500 to 1100 nm are shown in Fig. 8.22. The reflectivity maxima correspond to the PBG and demonstrate a blue-shift with the increase of the angle of incidence, which is typical for opals [40, 41]. The inset in Fig. 8.22 shows a linear dependence of the central PBG wavelength on $\sin^2(\theta)$ that stays in good agreement with the Bragg diffraction condition $\lambda = 2d_{111}\sqrt{\epsilon_{\text{eff}} - \sin^2\theta}$, where d_{111} is the crystal lattice parameter along the crystallographic direction [111] and ϵ_{eff} is the effective dielectric constant of the composite opal.

When studying the nonlinear optical spectroscopy in composite opals with YIG, the output of a nanosecond OPO laser system in the spectral range from 700 to 1100 nm with a pulse duration of about 4 ns and a peak intensity of 1 MW/cm^2 is used as the fundamental radiation. A Fresnel rhomb (placed in front of the sample)

Fig. 8.22 Reflectivity spectra of opal-Pt-YIG composite PC for various angles of incidence of the fundamental beam. *Inset*: dependence of the square of the PBG central wavelength λ^2 on $\sin^2(\theta)$
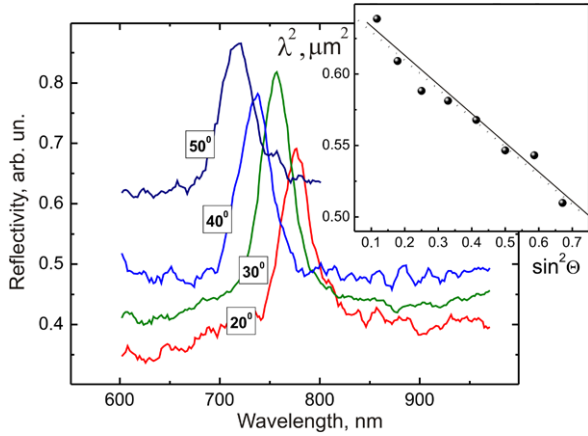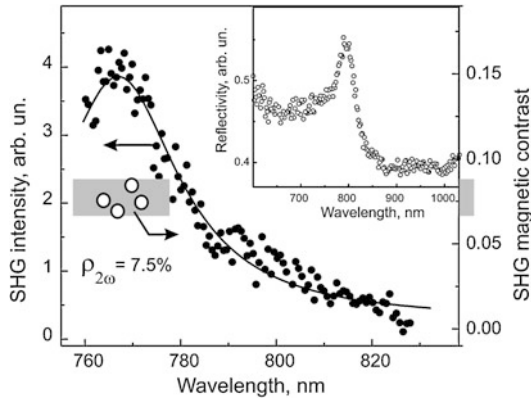
Fig. 8.23 Main panel: SHG intensity (*left scale*) and the NOMOKE (*right scale*) spectra in opal-YIG sample measured for $\theta = 20°$. *Insets*: reflectivity spectra of the same sample and for $\theta = 20°$

and Glan–Taylor polarizer (placed in the reflected from the sample beam) select the p-polarizations of both the fundamental and SHG waves. The SHG signal in the direction of the specular reflection is detected by a PMT and a boxcar integrator. The magnetic field of 2 kOe is applied to the sample in the geometry of the transversal magneto-optical Kerr effect, i.e. in the plane of the sample and perpendicular to the plane of incidence, as is shown schematically on the inset in Fig. 8.23. As has been described in the previous sections, this experimental geometry can lead only to the magnetization-induced changes the intensity of the reflected SHG.

Figure 8.23 shows the linear reflectivity spectra measured for $\theta = 20°$ for opal-YIG composite (without the Pt coverage) that reveals a spectral maximum centered at $\lambda \approx 790$ nm. SHG intensity spectrum of the same sample attained also for $\theta = 20°$ in the spectral vicinity of the PBG is shown in the main panel of Fig. 8.23. The spectral peak of the SHG intensity is centered around 770 nm, which corresponds to the PBG edge similarly to observed for Si-infiltrated opals [38]. Such behavior can be attributed to the fulfillment of the phase-matching conditions for the second harmonic generation, similarly to observed in 1D MPC and associated with a modified
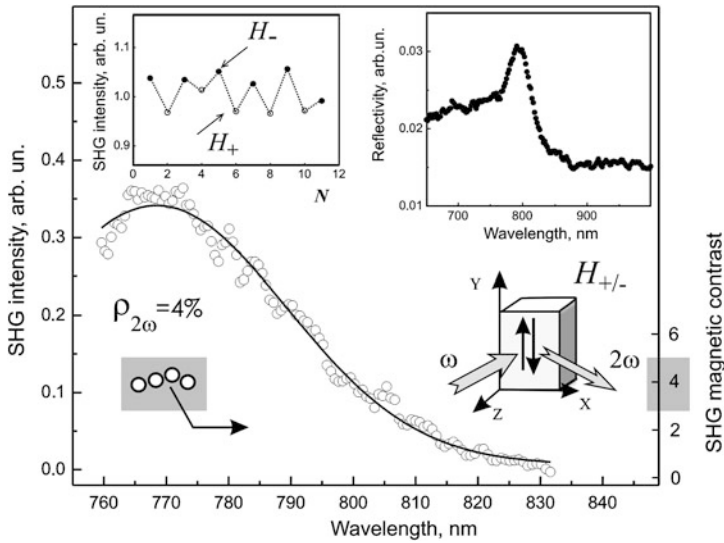
Fig. 8.24 Main panel: SHG intensity (*left scale*) and the NOMOKE (*right scale*) spectra in opal-P-t-YIG sample measured for $\theta = 20°$. *Inset*: reflectivity spectra of the same sample and for $\theta = 20°$

dispersion law of opal-based PC in this spectral region, which can be treated as nonlinear diffraction in 3D PC.

To reveal the magnetic state of opal-YIG composites, the transversal NOMOKE is studied for the two types of sample and the SHG contrast was measured for fixed wavelengths of the fundamental beam. The SHG intensity was first measured for one of the directions of the magnetic field for about 5000 laser pulses and gave the value $I_{2\omega}(H+)$, then the direction of H was reversed and the value $I_{2\omega}(H-)$ was measured. This procedure was repeated for dozens of times for each wavelength of the pump beam close to the spectral maximum of the SHG intensity. An example of the measured SHG intensities for the subsequent experiments is shown in Fig. 8.23, where N indicates the number of switching of the magnetic field. The values of the SHG intensity $I_{2\omega}(H+)$ and $I_{2\omega}(H-)$, averaged over the whole set of measurements, were taken to determine the SHG magnetic contrast.

The NOMOKE contrast for opal-YIG composites is shown in Fig. 8.23 (right scale for the main panel), the attained value is $\rho_{2\omega} = 4$ %. For comparison, in linear magneto-optical transversal Kerr effect for thin YIG films the analogous value is about 0.1 % or less.

Figure 8.24 shows the results of linear-optical (inset) and nonlinear-optical (main panel) spectroscopy of opal-Pt-YIG sample measured for $\theta = 20°$. The reflectivity maximum for the opal-Pt-YIG composite is twice as high as that for the opal-YIG composite under the same experimental conditions (insets in Figs. 8.23 and 8.24). This is probably related to a better quality of the SiO_2-Pt-YIG interfaces as compared with the SiO_2-YIG sample, as platinum prevents chemical reactions between yttrium oxide and the silica opal matrix. The main panel in Fig. 8.24 shows the SHG

spectrum, which reveals a sharp peak centered around 767 nm, which corresponds to the spectral position of the short-wavelength wing of the reflectivity spectrum. The mechanism of the SHG enhancement in the opal-Pt-YIG sample is expected to be the same as in the opal-YIG sample and is attributed to the realization of the phase-matching conditions for the SHG process at the PBG edge, while the increase of the SHG peak intensity is about one order of magnitude larger.

The SHG magnetic contrast in opal-Pt-YIG samples is about 7.5 % for the wavelengths close to the SHG spectral maximum. This value was obtained in the same way as for the SHG magnetic contrast for the opal-YIG composites and is shown in Fig. 8.24 for several wavelengths (the data refer to the right scale of the panel). Larger $\rho_{2\omega}$ values attained for opal-Pt-YIG composites as compared with Pt-free opal-YIG samples are probably caused by larger concentration of crystalline YIG inside the opal-Pt matrix due to the protective role of the Pt internal layers preventing strong chemical interaction of YIG precursors and the SiO_2 spheres. As the result, this leads to higher magnetization-induced nonlinear-optical effects in the sample.

Summing up, the SHG and NOMOKE spectroscopy are studied in 3D magnetophotonic crystals based on artificial opals infiltrated by yttrium–iron garnet. The existence of the crystalline magneto-optical YIG inside the 3D opal matrix is proven by XRD studies. The SHG magnetic contrast of 7.5 % is observed for the spectral edge of the photonic band gap of the composed magnetophotonic crystals.

8.6 Conclusions and Prospectives

In this chapter we have discussed the modern trends in nonlinear optics of novel photonic-band-gap systems based on conjugation of gyrotropic materials with broken time-reversal symmetry with photonic crystals approach yielding new possibilities to control the nonlinear generation and propagation of light that is flexible under external control impacts, such as a dc magnetic field. Nonlinear-optical analog of magneto-optical Kerr effect revealing itself in magnetization-induced changes of second- or third-harmonic intensity, polarization or relative phase is experimentally demonstrated in transversal, longitudinal and polar configuration of magnetic field application. One of the further developments of nonlinear magneto-optics in magnetophotonic crystals might be the search of similar effects in magnetoplasmonic crystals [42–44] and magnetoplasmonic nanostructures [45, 46] involving collective excitations of electron plasma. This might stimulate the integration of these new materials in modern telecommunication systems.

References

1. J.A. Armstrong, N. Bloembergen, J. Ducuing, P.S. Pershan, Phys. Rev. **127**, 1918 (1962)
2. N. Bloembergen, J. Sievers, Appl. Phys. Lett. **17**, 483 (1970)
3. S. Nakagawa, N. Yamada, N. Mikoshiba, D.E. Mars, Appl. Phys. Lett. **66**, 2159 (1995)
4. A.V. Balakin, V.A. Bushuev, N.I. Koroteev, B.I. Mantsyzov, I.A. Ozheredov, A.P. Shkurinov, D. Boucher, P. Masselin, Opt. Lett. **24**, 793 (1999)
5. M. Centini, G. D'Aguanno, M. Scalora, C. Sibilia, M. Bertolotti, M.J. Bloemer, C.M. Bowden, Phys. Rev. E **64**, 046606 (2001)
6. U. Pustogowa, W. Hubner, K.H. Bennemann, Phys. Rev. B **49**, 10031 (1994)
7. R.-P. Pan, H.D. Wei, Y.R. Shen, Phys. Rev. B **39** (1989)
8. J. Reif, J.C. Zink, C.-M. Schneider, J. Kirschner, Phys. Rev. Lett. **67**, 2878 (1991)
9. K. Bennemann, J. Magn. Magn. Mater. **200**, 697 (1999)
10. T.V. Murzina, E.M. Kim, R.V. Kapra, O.A. Aktsipetrov, A.F. Kravets, M. Inoue, S.V. Kuznetsova, M.V. Ivanchenko, V.G. Lifshits, Phys. Rev. B **73**, 140404(R) (2006)
11. B.B. Krichevtsov, V.V. Pavlov, R.V. Pisarev, JETP Lett. **49**, 535 (1989)
12. E. Popova, N. Keller, F. Gendron, M. Guyot, M.-C. Brianso, Y. Dumond, M. Tessier, J. Appl. Phys. **90**, 1422 (2001)
13. G. Petrocelli, S. Martellucci, M. Richetta, Appl. Phys. Lett. **63**, 3402 (1993)
14. V.N. Gridnev, V.V. Pavlov, R.V. Pisarev, A. Kirilyuk, Th. Rasing, Phys. Rev. B **63**, 184407 (2001)
15. R.V. Pisarev, B.B. Krichevtsov, V.N. Gridnev, V.P. Klin, D. Frohlich, C. Pahlke-Lerche, J. Phys. Condens. Matter **5**, 8621 (1993)
16. V.V. Pavlov, R.V. Pisarev, A. Kirilyuk, Th. Rasing, Phys. Rev. Lett. **78**, 2004 (1997)
17. O.A. Aktsipetrov, O.V. Braginskii, D.A. Esikov, Sov. J. Quantum Electron. **20**, 259 (1990)
18. I.L. Lyubchanskii, N.N. Dadoenkova, M.I. Lyubchanskii, Th. Rasing, J.-W. Jeong, S.-C. Shin, Appl. Phys. Lett. **76**, 2000 (2000)
19. S. Wittekoek, T.J.A. Popma, J.M. Robertson, P.F. Bongers, Phys. Rev. B **12**, 2777 (1975)
20. A.A. Fedyanin, O.A. Aktsipetrov, D. Kobayashi, K. Nishimura, H. Uchida, M. Inoue, J. Magn. Magn. Mater. **282**, 256 (2004)
21. S. Erokhin, Yu. Boriskina, A. Vinogradov, M. Inoue, D. Kobayashi, A. Fedyanin, M. Kochneva, E. Gan'shina, A. Granovsky, J. Magn. Magn. Mater. **300**, e257 (2006)
22. A.G. Zhdanov, A.A. Fedyanin, O.A. Aktsipetrov, D. Kobayashi, H. Uchida, M. Inoue, J. Magn. Magn. Mater. **300**, e253 (2006)
23. A.B. Khanikaev, A.V. Baryshev, M. Inoue, A.B. Granovsky, A.P. Vinogradov, Phys. Rev. B **72**, 035123 (2005)
24. H. Kato, T. Matsushita, A. Takayama, M. Egawa, K. Nishimura, M. Inoue, J. Appl. Phys. **93**, 3906 (2003)
25. A.K. Zvezdin, V.I. Belotelov, J. Opt. Soc. Am. B **22**, 228 (2005)
26. O.A. Aktsipetrov, E.M. Kim, R.V. Kapra, T.V. Murzina, A.F. Kravets, M. Inoue, S.V. Kuznetsova, M.V. Ivanchenko, V.G. Lifshits, Phys. Rev. B **73**, 140404 (2006)
27. K. Kemnitz, K. Bhattacharyya, J.M. Hicks, G.R. Pinto, K.B. Eisenthal, T.F. Heinz, Chem. Phys. Lett. **131**, 285 (1986)
28. T.V. Dolgova, A.A. Fedyanin, O.A. Aktsipetrov, K. Nishimura, H. Uchida, M. Inoue, J. Appl. Phys. **95**, 7330 (2004)
29. A.A. Fedyanin, T. Yoshida, K. Nishimura, G. Marowsky, M. Inoue, O.A. Aktsipetrov, J. Magn. Magn. Mater. **258–259**, 96 (2003)
30. O.A. Aktsipetrov, T.V. Dolgova, A.A. Fedyanin, R.V. Kapra, T.V. Murzina, K. Nishimura, H. Uchida, M. Inoue, Laser Phys. **14**, 685 (2004)
31. P. Guyot-Sionnest, Y.R. Shen, Phys. Rev. B **33**, 8254 (1986)
32. M. Inoue, K. Arai, T. Fujii, M. Abe, J. Appl. Phys. **85**, 5768 (1999)
33. M. Inoue, R. Fujikawa, A. Baryshev, A. Khanikaev, P.B. Lim, H. Uchida, O. Aktsipetrov, A. Fedyanin, T. Murzina, A. Granovsky, J. Phys. D, Appl. Phys. **39**, R151 (2006)

34. T.V. Murzina, I.E. Razdolski, O.A. Aktsipetrov, A.M. Grishin, S.I. Khartsev, J. Magn. Magn. Mater. **321**, 836 (2009)
35. A.A. Fedyanin, K. Nishimura, G. Marowsky, M. Inoue, O.A. Aktsipetrov, JETP Lett. **76**, 609 (2002)
36. O.A. Aktsipetrov, T.V. Dolgova, A.A. Fedyanin, T.V. Murzina, M. Inoue, K. Nishimura, H. Uchida, J. Opt. Soc. Am. B **22**, 176 (2005)
37. T.V. Murzina, E.M. Kim, R.V. Kapra, I.V. Moshnina, O.A. Aktsipetrov, D.A. Kurdyukov, S.F. Kaplan, V.G. Golubev, M.A. Bader, G. Marowsky, Appl. Phys. Lett. **88**, 022501 (2006)
38. A.A. Fedyanin, O.A. Aktsipetrov, D.A. Kurdyukov, V.G. Golubev, M. Inoue, Appl. Phys. Lett. **87**, 151111 (2005)
39. W. Stober, A. Fink, E. Bohn, J. Colloid Interface Sci. **26**, 62 (1968)
40. Y. Xia, B. Byron, Y. Yin, Y. Lu, Adv. Mater. **12**, 693 (2000)
41. C. Lopez, Adv. Mater. **15**, 1679 (2003)
42. A.A. Grunin, A.G. Zhdanov, A.A. Ezhov, E.A. Ganshina, A.A. Fedyanin, Appl. Phys. Lett. **97**, 261908 (2010)
43. A.A. Grunin, N.A. Sapoletova, K.S. Napolskii, A.A. Eliseev, A.A. Fedyanin, J. Appl. Phys. **111**, 07A948 (2012)
44. A.V. Chetvertukhin, A.V. Baryshev, H. Uchida, M. Inoue, A.A. Fedyanin, J. Appl. Phys. **111**, 07A946 (2012)
45. I.A. Kolmychek, T.V. Murzina, J. Wouters, T. Verbiest, O.A. Aktsipetrov, J. Opt. Soc. Am. B **29**(1), 138 (2012)
46. T.V. Murzina, I.A. Kolmychek, A.A. Nikulin, E.A. Gan'shina, O.A. Aktsipetrov, JETP Lett. **90**, 504 (2009)